CHALMERS
UNIVERSITY OF TECHNOLOGY

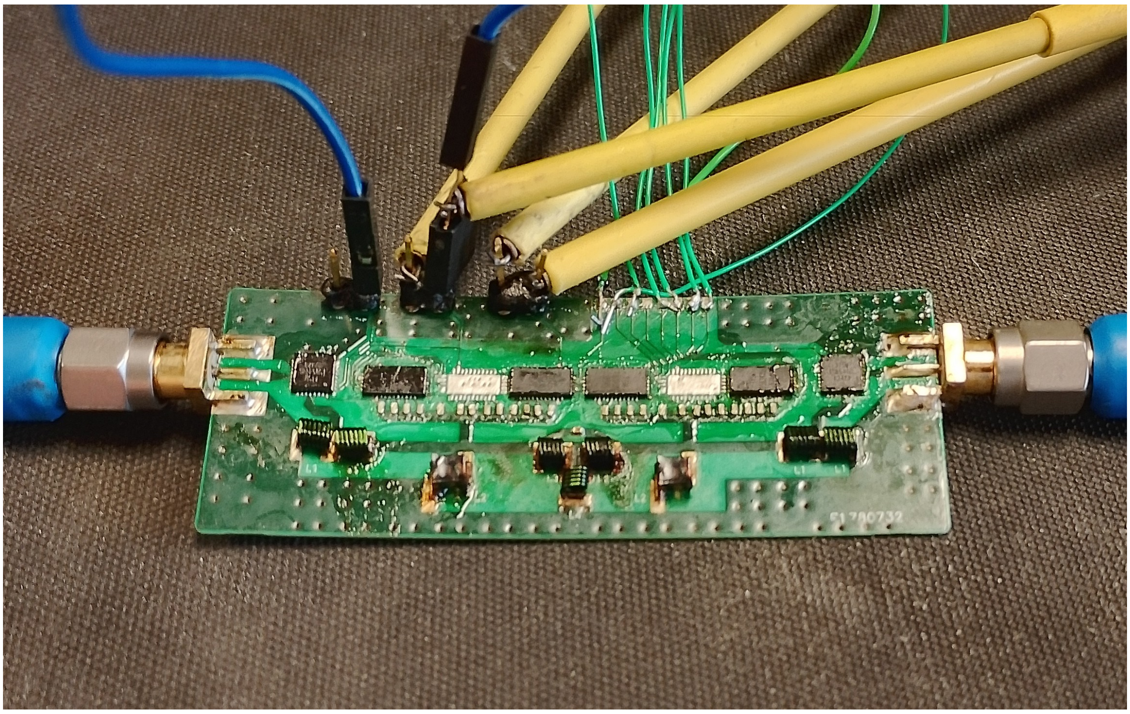

Practical Evaluation of GaN Switches in Tunable RF Filter Banks

Simulation, Fabrication, and Analysis of a High-Power 225–520 MHz Band-Pass Prototype

Master's thesis in Electrical Engineering

Fridolin Häggkvist

DEPARTMENT OF MICROTECHNOLOGY AND NANOSCIENCE
CHALMERS UNIVERSITY OF TECHNOLOGY
Gothenburg, Sweden 2026
www.chalmers.se

Master's thesis 2026

Practical Evaluation of GaN Switches in Tunable RF Filter Banks

Simulation, Fabrication, and Analysis of a High-Power 225–520 MHz Band-Pass Prototype

Fridolin Häggkvist

Department of Microtechnology and Nanoscience
Chalmers University of Technology
Gothenburg, Sweden 2026

Practical Evaluation of GaN Switches in Tunable RF Filter Banks
Simulation, Fabrication, and Analysis of a High-Power 225–520 MHz
Band-Pass Prototype
Fridolin Häggkvist

Supervisor: Dan Kuylenstierna, Department of Microtechnology and Nanoscience
Supervisor: Arne Øistein Olsen, Kongsberg Defence Communications
Supervisor: Nilsanu Pirak Sikku, Kongsberg Defence Communications
Examiner: Dan Kuylenstierna, Department of Microtechnology and Nanoscience

Master's Thesis 2026
Department of Microtechnology and Nanoscience
Chalmers University of Technology
SE-412 96 Gothenburg
Telephone +46 31 772 1000

Cover: Picture of filter board under test with two broken switches removed.

Typeset in LaTeX
Printed by Chalmers Reproservice
Gothenburg, Sweden 2026

Practical Evaluation of GaN Switches in Tunable RF Filter Banks
Simulation, Fabrication, and Analysis of a High-Power 225–520 MHz Band-Pass Prototype
FRIDOLIN HÄGGKVIST
Department of Microtechnology and Nanoscience
Chalmers University of Technology

Abstract

This thesis evaluates the use of Gallium Nitride (GaN) RF switches in a high-power tunable band-pass filter bank covering 225–520 MHz. The work includes filter synthesis, ADS optimization, EM simulation of critical PCB structures, prototype fabrication, VNA measurements, troubleshooting, and RF power testing.

The simulated second-order design covered the intended 225–520 MHz frequency range with fractional bandwidths close to 5% and insertion losses of approximately 3.6–5.5 dB. Measurements of the GaN switch evaluation board showed generally similar behavior to the supplied engineering model, although differences increased at higher frequencies.

The fabricated prototype could not be fully validated as a complete tunable filter bank because several switches failed during assembly and troubleshooting. The final measurements were therefore performed on a partially reworked circuit. The measured prototype showed the same general resonant behavior as the modified simulation, but with an approximately 10% downward frequency shift and worse matching. Troubleshooting and fault modeling indicated that incomplete RF grounding, rework-related parasitic capacitance, component faults, and assembly effects contributed to the difference between simulation and measurement.

The maximum RF power handling and $P_{1\mathrm{dB}}$ of the prototype could not be determined with the available measurement setup. EM simulation showed that the switch-node structure had an impedance of approximately 200 Ω, which increased the expected RF voltage stress across the switched capacitors. Capacitor voltage rating was therefore identified as a potential limitation for future high-power testing, but the limiting mechanism was not experimentally isolated.

The results show that GaN RF switches remain a possible alternative for high-power tunable filter applications, but the surrounding passive network, grounding, PCB parasitics, and measurement setup are important parts of the complete implementation. Future designs should use improved RF grounding, higher-voltage capacitors, lower switch-node impedance, and simpler staged prototypes before full high-power validation.

Keywords: GaN RF switches, tunable RF filters, filter banks, band-pass filters, RF power handling, switch parasitics, EM simulation, PCB prototyping

Acknowledgements

I would like to thank my supervisors Dan Kuylenstierna, Arne Øistein Olsen, and Nilsanu Pirak Sikku for their guidance, technical feedback, and support throughout the project. I would also like to thank Steve Nugent at Tagore Technology for supplying GaN switch samples and supporting material.
I am grateful to the student society ETA, and especially to Michal Dzialak, Tintin Axelsson, and Oscar Rosenlund, for practical help with board assembly, soldering, and laboratory work. Finally, I would like to thank the people around me who acted as sounding boards during the project.

Fridolin Häggkvist, Gothenburg, June 2026

List of Acronyms

Below is the list of acronyms that have been used throughout this thesis listed in alphabetical order:

ADS	Advanced Design System
BP	Band-Pass
BS	Band-Stop
CW	Continuous Wave
EM	Electromagnetic
FBW	Fractional Bandwidth
GaN	Gallium Nitride
FET	Field effect transistor
MEMS	Micro-Electro-Mechanical Systems
HP	High-Pass
IL	Insertion Loss
LP	Low-Pass
PCB	Printed Circuit Board
PIN-diode	P-type, Intrinsic, N-type diode
RF	Radio Frequency
RL	Return Loss
SMA	SubMiniature version A
VNA	Vector Network Analyzer

Nomenclature

Below is the nomenclature of symbols used throughout this thesis. Symbols are listed approximately in alphabetical order, with Latin symbols followed by Greek symbols.

Indices

i,j	General port, node, or resonator indices
n	Filter order or element index

Sets

–	No specific mathematical sets are used in this thesis

Parameters

A, B, C, D	Elements of an ABCD transmission matrix
C	Capacitance
C_k	Tuning capacitance in switched branch k
C_{eff}	Effective capacitance of a resonator, including selected and parasitic contributions
$C_{\text{eff,min}}, C_{\text{eff,max}}$	Minimum and maximum effective resonator capacitance over the tuning range
C_{fixed}	Fixed capacitance contributing to the resonator
C_{selected}	Total capacitance intentionally connected in the selected switch state
C_{off}	Off-state capacitance of an RF switch
$C_{\text{off,eq}}$	Equivalent off-state switch capacitance referred to the resonator node

$C_{\text{inactive},k}$	Residual capacitance contributed by inactive switched branch k
C_{PCB}	Equivalent PCB parasitic capacitance referred to the resonator node
C_{package}	Equivalent package parasitic capacitance referred to the resonator node
C_{par}	Aggregate parasitic capacitance in the first-order switched-branch model
C_p	Parallel capacitance in the band-pass filter transformation
C_s	Series capacitance in the band-pass filter transformation
f	Frequency
f_r	Resonant frequency
f_0	Center or resonant frequency
f_1, f_2	Lower and upper cutoff frequencies
$f_{\text{min}}, f_{\text{max}}$	Minimum and maximum resonant frequency over the tuning range
$f_{\text{meas}}, f_{\text{sim}}$	Measured and simulated resonant frequencies
f_{FOM}	Characteristic switch figure-of-merit frequency, $1/(2\pi R_{\text{on}} C_{\text{off}})$
FBW	Fractional bandwidth
g	Low-pass prototype element value
$g_0, g_1, \ldots, g_{n+1}$	Normalized low-pass prototype element values
I	Current
I_{rms}	Root-mean-square current
J	Admittance inverter value
j	Imaginary unit, $\sqrt{-1}$
L	Inductance
$L_{1,2}$	Original inverter inductance used in the bandwidth-compensation relation
L_{par}	Parasitic package and interconnect inductance of a switched branch
L_p	Parallel inductance in the band-pass filter transformation
L_s	Series inductance in the band-pass filter transformation
P	RF power
P_{loss}	Power dissipated by a resonator
$P_{\text{sw,on}}$	Approximate on-state conduction loss in an RF switch

Q	Quality factor
Q_C	Capacitor quality factor
$Q_{C,k}$	Effective quality factor associated with switched capacitor branch k
Q_u	Unloaded resonator quality factor
R	Resistance or reference load resistance
R_on	On-state resistance of an RF switch
$R_{\mathrm{ESR},k}$	Equivalent series resistance of tuning capacitor branch k
$R_{\mathrm{layout},k}$	Effective series resistance associated with PCB interconnects in branch k
$R_{s,C}$	Equivalent series resistance of a capacitor
$R_{s,k}$	Total first-order series loss resistance of switched branch k
S_{11}	Input reflection coefficient
S_{12}	Reverse transmission coefficient
S_{21}	Forward transmission coefficient
S_{22}	Output reflection coefficient
V	Voltage
V_pk	Peak voltage
V_rms	Root-mean-square voltage
V_pp	Peak-to-peak voltage
W_C	Energy stored in a capacitor
W_stored	Energy stored in a resonator
Y	Admittance
Y_0	Reference admittance
Z	Impedance
Z_0	Reference impedance, typically 50 Ω
Z_sw	State-dependent RF-switch impedance in the first-order branch model
$Z_\mathrm{sw,on}$	First-order on-state switch impedance
$Z_\mathrm{sw,off}$	First-order off-state switch impedance
ΔC	Change in capacitance
ΔC_eff	Change in effective resonator capacitance
$\Delta f, \Delta f_0$	Change in frequency or resonant frequency
ΔL	Change in effective resonator inductance
ϵ_r	Relative permittivity

γ_0	System impedance used in the filter transformation equations
λ	Wavelength
μ_r	Relative permeability
ω	Angular frequency
ω_0	Angular center frequency
ω_1, ω_2	Lower and upper angular cutoff frequencies
ω_p	Compensation frequency used in the absolute-bandwidth inverter relation
Ω	Normalized low-pass prototype frequency variable
Ω_c	Normalized cutoff frequency

Variables

S_{ij}	Measured or simulated scattering parameter from port j to port i
Z_{in}	Input impedance
Z_{node}	Simulated or measured impedance at a switch-node structure

Contents

List of Figures

List of Tables

1

Introduction

1.1 Motivation and Problem Statement

Modern wireless communication, radar, and electronic-warfare systems depend on the ability to transmit and receive signals selectively in an increasingly congested radio-frequency spectrum. RF filters are therefore essential in both transmitters and receivers, where they suppress unwanted frequency components, limit out-of-band interference, and protect sensitive circuit stages. Important filter characteristics include insertion loss, return loss, bandwidth, selectivity, linearity, and power handling [1, 2, 3].

A fixed-frequency filter is often insufficient in systems that must operate over a wide frequency range. Reconfigurable filtering can instead be achieved using continuously tunable filters, discretely tunable filters, switched filter banks, or combinations of these architectures [4, 5, 6]. A tunable filter changes electrical parameters within a shared filter network, whereas a switched filter bank routes the RF signal through one of several separate filter branches. Hybrid systems combine coarse switched-band selection with tuning within the selected branch.

Recent implementations illustrate several levels of integration. Fully monolithic switched filter banks have combined semiconductor switches, filter branches, and digital control functions in a single GaAs MMIC [7]. Other work has merged the switching and filtering functions into a common band-pass switch building block, reducing the need for separate switch and filter networks [8]. Clocked N-path architectures provide another route to integrated frequency tuning: CMOS implementations can cover wide tuning ranges with compact chip area, while a measured GaN MMIC N-path filter has demonstrated substantially higher in-band power handling [9, 10]. Hybrid implementations remain important in practice, including PCB filter banks using packaged switch ICs and system-in-package modules that combine SOI switches with acoustic filters [11, 12].

These integrated examples are not direct replacements for the architecture studied in this thesis. Their operating frequencies, filter mechanisms, semiconductor processes, power levels, and intended applications differ. They nevertheless show the main implementation choices: integrating the complete filter on a semiconductor die, integrating separate filter and switch dies in one package, or combining packaged switches with PCB-based passive resonators. The present work investigates the third approach, with particular emphasis on high RF power and operation in the VHF/UHF range.

The complete filter-bank architecture considered in this project is intended to cover 30 MHz to 520 MHz. The system is divided into several frequency sections, each containing a finite number of selectable filter states. The complete system can therefore be described as a switched multiband filter bank, while each individual section is a discretely tunable filter.

Such a system must maintain acceptable insertion loss, selectivity, bandwidth, and power handling over a large number of switching states. This is challenging because the switching elements, passive components, PCB interconnects, and grounding structures all introduce losses and parasitic reactances. Their effects vary with frequency and switching state and may cause significant differences between ideal simulations and the measured implementation.

1.2 Societal, Ethical, and Environmental Considerations

The filter technology investigated in this thesis is relevant to radio communication, radar, and electronic-warfare systems and therefore has both civilian and defence-related applications. The work consequently has a dual-use character. The thesis evaluates RF hardware and does not involve human subjects, personal data, or autonomous decision-making. An important ethical consideration is therefore the responsible handling and reporting of technical information supplied by the industrial partner and component manufacturer, while maintaining reproducibility and scientific transparency within the information that may be published.

From an environmental perspective, the prototype itself has a limited direct impact because only a small number of PCBs and electronic components were manufactured. However, repeated prototype iterations, damaged semiconductor devices, PCB fabrication, and laboratory energy use generate material and electronic waste. Improved simulation, staged single-resonator prototypes, and design verification before assembly could reduce unnecessary hardware iterations. At system level, lower-loss filtering can also reduce dissipated RF power, although the environmental impact of a complete end application was outside the scope of this thesis.

No attempt is made in this work to assess particular military applications or their societal consequences. Nevertheless, the dual-use nature of the technology should be considered when deciding how a future implementation is developed and deployed.

1.3 PIN-Diode Reference and GaN Motivation

PIN diodes are widely used as switching and tuning elements in high-power RF systems. When forward biased, a PIN diode behaves approximately as a current-controlled RF resistance. When reverse biased, it behaves primarily as a small capacitance. This combination of low on-state resistance, low off-state capacitance, and relatively high RF power capability has made the PIN diode an established solution for high-power switching applications.

The required bias conditions depend strongly on the operating conditions. In the conducting state, sufficient forward current is required to obtain low resistance and acceptable linearity. In the blocking state, sufficient reverse bias is needed to prevent unwanted conduction during the positive portion of the RF waveform. The minimum reverse-bias voltage depends on peak RF voltage, operating frequency, duty factor, load mismatch, diode properties, and circuit topology; it cannot generally be determined from average RF power alone [13, 14].

High-voltage bias circuitry is nevertheless used in several practical PIN-diode-tuned filters. The Netcom 5588 digitally tunable filter, for example, specifies a 100 V bias input and uses high-voltage drivers for its PIN-diode tuning network [15]. Documentation for the related Netcom 5590 describes a programmable PIN-diode filter supplied from a nominal external voltage of approximately 150 V [16]. In the reference implementation that motivated this thesis, reverse-bias voltages exceeding 200 V were also reportedly used at RF test powers of approximately 5 W [17]. This value is specific to that implementation and is not a general requirement for all PIN-diode switches.

High-voltage bias requirements increase system complexity. Additional power converters, bias drivers, isolation components, and PCB spacing may be required. The bias network and switching devices also add resistance, capacitance, and parasitic coupling that can increase insertion loss and alter the filter response.

Gallium-nitride transistor switches provide a possible alternative. GaN devices can combine high breakdown voltage, low on-state resistance, and relatively small off-state capacitance, making them attractive for wideband and high-power RF switching [18]. Recent measurements of a heterogeneous GaN/RF-SOI SPDT switch reported different limits under continuous-wave and pulsed excitation, illustrating that thermal accumulation can be as important as instantaneous voltage or current stress [19]. Device linearity may also depend on substrate properties, while switch parameters and losses vary with temperature [20, 21]. GaN technology must therefore be evaluated in the intended circuit rather than assumed to provide better performance under all conditions.

Replacing PIN diodes with GaN switches also does not remove all power limitations. Resonant filters can produce voltages and currents within the passive components that are substantially greater than those at the external 50 Ω ports. Capacitor voltage ratings, inductor current ratings, component losses, grounding, solder joints, and local heating may therefore limit the filter power handling before the GaN switch itself reaches its specified limit.

1.4 Aim and Research Questions

The aim of this thesis is to evaluate whether commercially available GaN RF switches can be used in a high-power, discretely tunable band-pass-filter section intended for a wider switched multiband filter bank.

The work evaluates the RF performance of a fabricated prototype and investigates the agreement between circuit-level simulations, manufacturer component models, electromagnetic simulations, and measurements. Particular attention is given to insertion loss, bandwidth, selectivity, tuning accuracy, and RF power handling.

The work is guided by the following research questions:

- What insertion loss, return loss, bandwidth, and stopband rejection can the GaN-switched filter achieve across the 225 MHz to 520 MHz tuning range?
- How accurately do circuit-level, component-model, and electromagnetic simulations predict the measured response of the fabricated prototype?
- Which mechanisms limit the continuous-wave and peak RF power handling of the prototype?
- To what extent are the measured limitations attributable to the GaN switches rather than to the passive components, bias networks, PCB layout, grounding, or thermal implementation?

1.5 Scope and Limitations

The complete proposed filter-bank system is intended to cover 30 MHz to 520 MHz. Owing to the time available for the project, only the higher-frequency section covering 225 MHz to 520 MHz was designed, fabricated, and characterised.

The work is a proof-of-concept investigation rather than the development of a production-ready filter bank. It focuses on the practical feasibility of the GaN-switched architecture and on identifying the dominant limitations of the implementation.

The investigation includes:

- synthesis and circuit-level simulation of the filter;
- simulation using manufacturer component models;
- electromagnetic simulation of selected PCB structures;
- fabrication and small-signal characterisation of the prototype;
- investigation of RF power handling and failure mechanisms; and
- comparison between simulated and measured behaviour.

The work does not include complete qualification for production use, long-term reliability testing, environmental testing, or implementation of the complete 30 MHz to 520 MHz filter bank. The comparison with PIN-diode technology is therefore based on published results, commercial specifications, the motivating reference implementation, and the measured behaviour of the GaN prototype rather than on two otherwise identical fabricated filters.

1.6 Thesis Outline

Chapter 2 presents the filter theory required to understand the design, including resonator Q, switch non-idealities, parasitic capacitance and inductance, tuning behavior, and RF power stress. Chapter 3 describes the selected filter topology, component and switch modeling, electromagnetic simulation, PCB fabrication, measurement procedure, and the prototype troubleshooting and fault-isolation process used during experimental testing. Chapter 4 presents the simulated and measured results and gives a concise summary of the answers to the research questions. Chapter 5 discusses the main findings, compares the results with the project targets, examines the discrepancy between simulation and measurement, and identifies improvements for future implementations.

2

Theory

This chapter presents the theory needed to understand the design and measured behavior of the tunable band-pass filter investigated in this thesis. The focus is therefore not only on ideal filter synthesis, but also on the non-ideal mechanisms that become important when discrete resonators are tuned using RF switches. In particular, the on-state resistance R_{on}, off-state capacitance C_{off}, passive-component Q-factors, PCB parasitics, and resonator-node impedance determine how closely the implemented filter can approach the response predicted by an ideal synthesis.

2.1 Band-pass filter synthesis

A narrowband band-pass filter can be synthesized from a normalized low-pass prototype. The prototype element values g_i determine the required coupling and resonator values for a selected approximation, such as Butterworth or Chebyshev [3, 2]. A second-order Chebyshev response is particularly relevant to this work because it provides a sharper transition than a Butterworth response of the same order while requiring only two resonators.

For a band-pass response, the center angular frequency is

$$\omega_0 = \sqrt{\omega_1 \omega_2}, \tag{2.1}$$

where ω_1 and ω_2 are the lower and upper band-edge frequencies. The fractional bandwidth is

$$\mathrm{FBW} = \frac{\omega_2 - \omega_1}{\omega_0}. \tag{2.2}$$

The normalized low-pass frequency variable can be mapped to a band-pass response according to [3, 2]

$$\Omega = \frac{\Omega_c}{\mathrm{FBW}} \left(\frac{\omega}{\omega_0} - \frac{\omega_0}{\omega} \right), \tag{2.3}$$

where Ω_c is the normalized prototype cut-off frequency.

For a system impedance γ_0 and prototype value g, the corresponding series-resonator

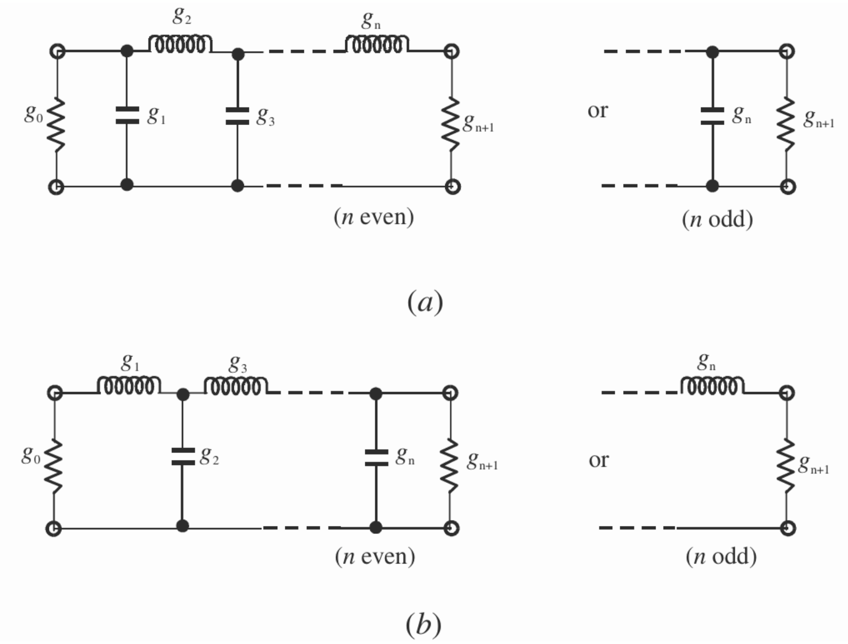

Figure 2.1: Low-pass prototype for an all-pole filter. Figure adapted from Hong and Lancaster [3].

values are

$$L_s = \frac{\Omega_c \gamma_0 g}{\mathrm{FBW}\, \omega_0}, \tag{2.4}$$

$$C_s = \frac{\mathrm{FBW}}{\omega_0 \Omega_c \gamma_0 g}, \tag{2.5}$$

while a parallel resonator can be written as

$$C_p = \frac{\Omega_c g}{\mathrm{FBW}\, \omega_0 \gamma_0}, \tag{2.6}$$

$$L_p = \frac{\mathrm{FBW}\, \gamma_0}{\omega_0 \Omega_c g}. \tag{2.7}$$

These expressions describe an ideal filter. In the implemented circuit, the effective resonator values also contain switch and layout parasitics. The synthesized component values should therefore be interpreted as starting values rather than as the final physical component values.

2.1.1 Filter order and approximation

Increasing the filter order improves the ideal stopband roll-off, but each additional resonator also introduces another finite-Q element and additional coupling structures. The practical insertion loss and sensitivity to component tolerances therefore generally increase with filter order [3, 2].

A Chebyshev response allows a controlled amount of passband ripple in exchange for a sharper transition. For the tunable filter in this thesis, the second-order topology provides a useful compromise between selectivity, insertion loss, tuning complexity, and the number of switched resonator branches.

2.2 Admittance inverters and parallel resonators

A direct band-pass realization can contain both series and parallel resonators. In a switched filter, a series resonator is inconvenient because the RF switch and its parasitic resistance can be placed directly in the main signal path. Admittance inverters, or J-inverters, can instead be used to realize a band-pass network using parallel resonators [3].

An ideal J-inverter has the ABCD matrix

$$\begin{bmatrix} A & B \\ C & D \end{bmatrix} = \begin{bmatrix} 0 & \mp\dfrac{1}{jJ} \\ \pm jJ & 0 \end{bmatrix}, \tag{2.8}$$

which gives the admittance transformation

$$Y_1 = \frac{J^2}{Y_2}. \tag{2.9}$$

Around the design frequency, a practical inverter can be approximated by an inductive element according to

$$L_J \approx \frac{1}{\omega_0 J}. \tag{2.10}$$

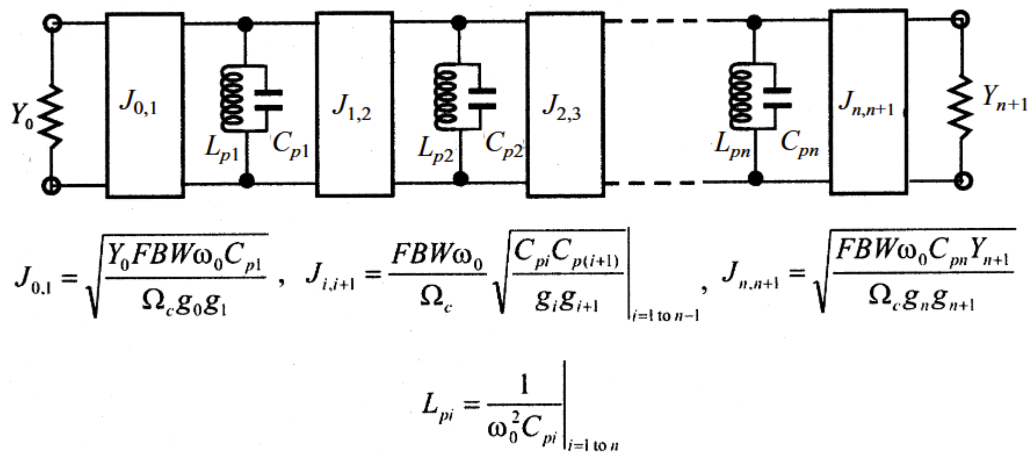

Figure 2.2: Example of a J-inverter implementation for a band-pass filter [3].

For a second-order two-port filter, three inverter sections are required: one between the source and the first resonator, one between the resonators, and one between the second resonator and the load. The inverters are frequency dependent and non-ideal when implemented using physical inductors and PCB interconnects. Their parasitic capacitance, series resistance, and coupling to surrounding structures therefore affect both the center frequency and the bandwidth.

2.3 Quality factor and dissipation loss

The Q-factor relates the energy stored in a resonator to the energy dissipated per RF cycle. A general definition is [1]

$$Q = \omega_0 \frac{W_{\text{stored}}}{P_{\text{loss}}} = 2\pi f_0 \frac{W_{\text{stored}}}{P_{\text{loss}}}. \tag{2.11}$$

It is useful to distinguish between component Q, unloaded resonator Q, and loaded Q. For a narrowband loaded resonator,

$$Q_{\text{L}} \approx \frac{f_0}{\text{BW}} = \frac{1}{\text{FBW}}, \tag{2.12}$$

whereas the unloaded Q, Q_{u}, describes internal dissipation before loading by the external source and load. If several independent loss mechanisms are represented using partial Q-values referred to the same stored energy, their contributions add as

$$\frac{1}{Q_{\text{u}}} = \frac{1}{Q_1} + \frac{1}{Q_2} + \cdots . \tag{2.13}$$

For a practical inductor with equivalent series resistance $R_{s,L}$,

$$Q_L \approx \frac{\omega L}{R_{s,L}}, \tag{2.14}$$

and for a capacitor with equivalent series resistance $R_{s,C}$,

$$Q_C \approx \frac{1}{\omega C R_{s,C}}. \tag{2.15}$$

These relations show directly why passive-component loss becomes increasingly important in a narrowband filter.

For a narrowband coupled-resonator filter, the dissipation loss can be estimated from the prototype values according to [2]

$$\text{Loss}_{\text{dB}} \approx \frac{4.343}{\text{FBW}\, Q_{\text{u}}} \sum_x g_x. \tag{2.16}$$

The approximation shows that a small fractional bandwidth requires a high unloaded resonator Q to maintain low insertion loss. In the design procedure used later in this thesis, this relation is used to translate the specified insertion-loss and bandwidth targets into a required resonator-Q level. For the approximately 5 % fractional bandwidth considered in this work, even a moderate reduction in resonator Q therefore has a direct and visible effect on the achievable passband loss.

2.4 RF-switch non-idealities in a tuned resonator

Several switch technologies can be used in reconfigurable RF networks, including PIN diodes, RF MEMS, GaAs FETs, SOI switches, and GaN RF switches. Their suitability depends on insertion loss, isolation, linearity, power handling, bias complexity, switching speed, and reliability [22, 8, 19]. For the present work, the most important small-signal switch parameters are the on-state resistance R_{on} and off-state capacitance C_{off}, because they directly affect resonator loss and the effective tuning capacitance.

2.4.1 First-order model of a switched tuning branch

A switched capacitor branch can be represented to first order by a switch impedance Z_{sw} in series with a tuning capacitor C_k, together with parasitic capacitance from the RF node to ground. The switch impedance is state dependent and can be approximated as

$$Z_{\mathrm{sw,on}} \approx R_{\mathrm{on}} + \mathrm{j}\omega L_{\mathrm{par}}, \tag{2.17}$$

$$Z_{\mathrm{sw,off}} \approx \frac{1}{\mathrm{j}\omega C_{\mathrm{off}}}, \tag{2.18}$$

where L_{par} represents package and interconnect inductance. In a more complete model, finite off-state resistance, pad capacitance, package capacitance, bias-network impedance, and frequency- and temperature-dependent device parameters must also be included.

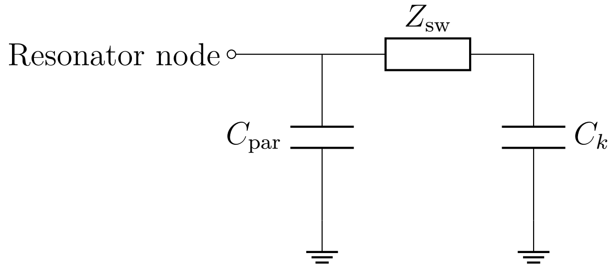

Figure 2.3: First-order equivalent circuit of one switched tuning branch. In the on state, Z_{sw} is dominated by R_{on} and package/interconnect inductance. In the off state, the branch remains coupled through C_{off}. The capacitance C_{par} represents PCB, pad, and package capacitance referred to the resonator node.

Figure 2.3 is intentionally a first-order model. It is not intended to replace the manufacturer's engineering model, but it makes clear how the same physical switch can influence the filter differently in its two states. In the on state, the dominant effect is additional series loss. In the off state, the dominant effect is residual capacitive loading. Both effects are coupled to the PCB parasitics surrounding the resonator node.

The product

$$R_{\mathrm{on}} C_{\mathrm{off}} \tag{2.19}$$

is commonly used as a first-order switch technology figure of merit [21]. An equivalent characteristic frequency can be written as

$$f_{\mathrm{FOM}} = \frac{1}{2\pi R_{\mathrm{on}} C_{\mathrm{off}}}. \tag{2.20}$$

This frequency should not be interpreted as a hard operating-frequency limit. Rather, it summarizes the trade-off between conduction loss in the on state and capacitive loading in the off state.

The TS63430D used in this work is specified with a typical R_{on} of $0.50\,\Omega$ and a typical C_{off} of $500\,\mathrm{fF}$ in the manufacturer's current product brief [23]. These values are used below only as first-order magnitude checks. The engineering model used during the circuit design contains a more complete representation of the device and should be used for accurate state- and frequency-dependent simulation.

2.4.2 Effect of on-state resistance on resonator Q

When a tuning capacitor is connected through an RF switch, the on-state resistance becomes part of the loss resistance of that branch. For a switched capacitor C_k, a first-order series-loss model is

$$R_{s,k} \approx R_{\mathrm{ESR},k} + R_{\mathrm{on},k} + R_{\mathrm{layout},k}. \tag{2.21}$$

The effective Q of that capacitor branch is then approximately

$$Q_{C,k} \approx \frac{1}{\omega C_k R_{s,k}}. \tag{2.22}$$

Equation 2.22 provides the direct connection between switch resistance and filter performance. Increasing R_{on} increases RF dissipation, lowers the Q associated with the switched branch, and contributes to a lower unloaded resonator Q. Through Eq. 2.16, this increases passband insertion loss. The additional damping can also alter the depth and width of the resonance, meaning that R_{on} can influence both S_{21} and S_{11} rather than appearing only as a constant series attenuation.

A useful magnitude check can be made using the largest switched capacitance used in the design. For $C_k = 10\,\mathrm{pF}$, $f = 520\,\mathrm{MHz}$, and $R_{\mathrm{on}} = 0.50\,\Omega$, while temporarily neglecting capacitor ESR and layout loss,

$$Q_{C,k}^{(R_{\mathrm{on}})} \approx \frac{1}{2\pi(520\,\mathrm{MHz})(10\,\mathrm{pF})(0.50\,\Omega)} \approx 61. \tag{2.23}$$

This value is not the unloaded Q of the complete resonator. The total resonator Q depends on the inductor loss, capacitor ESR, layout loss, coupling, and the fraction of the stored electric energy associated with each switched branch. Nevertheless, the result shows that the switch resistance alone produces a branch-Q limit of the same order of magnitude as the resonator-Q target derived later in the design procedure. The contribution of R_{on} should therefore not be assumed negligible, particularly for the larger tuning capacitors and at the upper end of the tuning range.

2.4.3 Effect of off-state capacitance

An open RF switch is not an ideal open circuit. Its off-state capacitance provides a finite RF path and loads the resonator even when the corresponding tuning branch is disabled. For the common case in which C_{off} is effectively in series with an inactive tuning capacitor C_k, the remaining branch capacitance is approximately

$$C_{\text{inactive},k} \approx \frac{C_{\text{off}} C_k}{C_{\text{off}} + C_k}. \tag{2.24}$$

If $C_k \gg C_{\text{off}}$, the inactive branch approaches C_{off} rather than zero capacitance. The branch therefore continues to affect the resonator in the nominal off state.

Using the typical TS63430D value $C_{\text{off}} = 0.50\,\text{pF}$ and a $10\,\text{pF}$ tuning capacitor gives

$$C_{\text{inactive}} \approx \frac{(0.50\,\text{pF})(10\,\text{pF})}{0.50\,\text{pF} + 10\,\text{pF}} \approx 0.476\,\text{pF}. \tag{2.25}$$

Thus, a branch containing a relatively large tuning capacitor still contributes almost $0.5\,\text{pF}$ in this simplified off-state model. This is significant because the high-frequency filter states use small total resonator capacitances, making sub-picofarad parasitic contributions a non-negligible part of the effective capacitance.

If the effective capacitance of a resonator is written as

$$C_{\text{eff}} = C_{\text{fixed}} + C_{\text{selected}} + C_{\text{off,eq}} + C_{\text{PCB}} + C_{\text{package}}, \tag{2.26}$$

where the parasitic terms are interpreted as first-order equivalent capacitances referred to the resonator node, the ideal LC resonance becomes

$$f_0 = \frac{1}{2\pi\sqrt{LC_{\text{eff}}}}. \tag{2.27}$$

The maximum tuning ratio of a resonator with approximately constant inductance is therefore

$$\frac{f_{\max}}{f_{\min}} = \sqrt{\frac{C_{\text{eff,max}}}{C_{\text{eff,min}}}}. \tag{2.28}$$

A fixed parasitic capacitance or large C_{off} increases $C_{\text{eff,min}}$ and therefore compresses the achievable tuning range. This effect becomes particularly important in the high-frequency states, where the intended tuning capacitance is smallest. Off-state capacitance can also reduce isolation between nominally inactive and active branches and can therefore cause state-to-state interaction.

2.4.4 Parasitic capacitance and resonance sensitivity

Equation 2.27 gives a useful first-order sensitivity relation. A small change in resonator inductance and capacitance gives

$$\frac{\Delta f_0}{f_0} \approx -\frac{1}{2}\left(\frac{\Delta L}{L} + \frac{\Delta C_{\text{eff}}}{C_{\text{eff}}}\right). \tag{2.29}$$

If the inductance is assumed to remain approximately unchanged,

$$\frac{\Delta f_0}{f_0} \approx -\frac{1}{2}\frac{\Delta C_{\mathrm{eff}}}{C_{\mathrm{eff}}}. \tag{2.30}$$

For larger deviations, it is preferable to use the exact ratio obtained from Eq. 2.27. If a measured resonance occurs at $0.90 f_{\mathrm{sim}}$ and the effective inductance is assumed unchanged, then

$$\frac{C_{\mathrm{eff,meas}}}{C_{\mathrm{eff,sim}}} = \left(\frac{f_{\mathrm{sim}}}{f_{\mathrm{meas}}}\right)^2 = \left(\frac{1}{0.90}\right)^2 \approx 1.235. \tag{2.31}$$

A 10 % downward frequency shift therefore corresponds, in this simplified interpretation, to approximately 23.5 % larger effective capacitance. This relation is useful later when interpreting the measured frequency shift. It does not prove that additional capacitance is the only cause: an increase in effective inductance, changed coupling, grounding errors, component tolerances, or rework can produce part of the same shift. The calculation instead provides an order-of-magnitude test of whether the required parasitic change is physically plausible.

The same sensitivity explains why a nominal tuning step ΔC does not produce a constant frequency step:

$$\frac{\Delta f}{f} \approx -\frac{1}{2}\frac{\Delta C}{C_{\mathrm{eff}}}. \tag{2.32}$$

The frequency change caused by a given switched capacitance therefore depends on the total capacitance already present in that state.

2.4.5 Parasitic inductance and self-resonance

The switch package, component pads, vias, and short PCB traces also introduce parasitic inductance. Together with C_{off} and the PCB capacitance, this can form unintended resonances. A physical capacitor or inductor must therefore be used sufficiently below its self-resonance frequency for the intended lumped-element model to remain valid. Near self-resonance, the component impedance can differ strongly from the ideal $1/(\mathrm{j}\omega C)$ or $\mathrm{j}\omega L$ response.

2.5 Bandwidth, coupling, and tuning

A tunable filter can be designed to maintain approximately constant fractional bandwidth or approximately constant absolute bandwidth. From Eq. 2.2, constant fractional bandwidth implies that the absolute bandwidth increases with center frequency. For a narrowband resonator, Eq. 2.12 also shows that a nearly constant loaded Q corresponds to nearly constant fractional bandwidth.

A fixed physical coupling network does not generally maintain identical coupling over a wide tuning range. The reactance of an inductive J-inverter varies with frequency, while the resonator impedance is also changed by the selected capacitance and by switch parasitics. Consequently, both the loaded Q and the fractional bandwidth can vary between tuning states even if the same low-pass prototype is used for every state.

One approach to an approximately constant absolute bandwidth is to compensate the inverter reactance. For the method investigated in this work, a parallel capacitor can be added to the inverter inductance. The compensated values can be written as [22]

$$L_p = L_{1,2}\sqrt{1 - \frac{\omega_p^2}{\omega_0^2}}, \qquad C_p = \frac{1}{\omega_p^2 L_p}, \tag{2.33}$$

where $L_{1,2}$ is the original inverter inductance and ω_p is the compensation frequency defined by the chosen synthesis method. In practice, finite component Q and parasitic capacitances prevent the bandwidth from following the ideal synthesis exactly, and circuit/EM optimization is therefore required.

2.6 Impedance and RF power stress

The external RF ports are referenced to a characteristic impedance, typically $50\,\Omega$, but the impedance inside a resonant filter can be substantially higher or lower. For a purely resistive local impedance Z and RMS voltage,

$$P = \frac{V_{\mathrm{rms}}^2}{Z}, \qquad V_{pp} = \sqrt{8PZ}. \tag{2.34}$$

Thus, for the same RF power, a high-impedance node produces a larger voltage swing.

As an order-of-magnitude example, consider an RF power of 5 W. At a $50\,\Omega$ resistive node,

$$V_{\mathrm{pk},50} = \sqrt{2PZ} \approx 22.4\,\mathrm{V}, \qquad V_{pp,50} \approx 44.7\,\mathrm{V}. \tag{2.35}$$

If the same power is associated with a $200\,\Omega$ local impedance,

$$V_{\mathrm{pk},200} \approx 44.7\,\mathrm{V}, \qquad V_{pp,200} \approx 89.4\,\mathrm{V}. \tag{2.36}$$

The local voltage is therefore doubled when the impedance increases from $50\,\Omega$ to $200\,\Omega$ for the same power. This simple calculation is directly relevant to switched resonator nodes, where EM simulation can reveal impedances substantially different from the external system impedance.

The calculation in Eq. 2.36 should not be interpreted as the exact voltage across an individual capacitor or switch. The local impedance is generally complex, and the distribution of voltage among the resonator elements depends on the complete network. Resonance can further increase internal reactive voltage and current because energy is repeatedly exchanged between the inductor and capacitor. From Eq. 2.11, the stored energy can be written as

$$W_{\mathrm{stored}} = \frac{QP_{\mathrm{loss}}}{\omega_0}. \tag{2.37}$$

For a capacitor that stores a significant part of this energy,

$$W_C = \frac{1}{2} C V_{\text{pk}}^2. \tag{2.38}$$

These relations show why the voltage across a switched capacitor or an off-state switch can exceed the voltage estimated directly from the external $50\,\Omega$ port power.

In the on state, the switch also dissipates approximately

$$P_{\text{sw,on}} \approx I_{\text{rms}}^2 R_{\text{on}}. \tag{2.39}$$

Self-heating can in turn change the switch parameters. Temperature-dependent GaN-switch measurements have shown that small-signal switch parameters can vary with operating condition, which limits the accuracy of a single room-temperature model at elevated RF power [21]. Large-signal measurements of GaN-based switches have also shown that continuous-wave and pulsed power limits can differ because of heat accumulation [19].

Power handling of the complete filter is therefore not set by the semiconductor switch alone. Capacitor voltage rating, inductor current rating, solder joints, PCB return paths, thermal conditions, and local field concentration can all become limiting mechanisms.

2.7 PCB parasitics and electromagnetic implementation

At RF frequencies, the physical implementation is part of the circuit. Component pads, traces, vias, ground planes, and bias structures add capacitance and inductance and can modify the effective impedance of a resonator node [1, 3]. These effects are particularly important in the switched capacitor bank because several nominally inactive branches remain physically connected to the same RF node.

The characteristic impedance and electrical length of a PCB trace depend on the trace geometry, substrate thickness, and effective permittivity. A short interconnect can often be approximated as a lumped parasitic element, while an electrically longer trace must be treated as a transmission line. The transition between the two descriptions is gradual rather than abrupt.

For the switch node, parasitic capacitance to ground is especially important because it enters directly into C_{eff} in Eq. 2.26. The resulting frequency shift can then be estimated from Eq. 2.30. Parasitic series inductance changes the effective inverter and resonator inductances and can similarly be interpreted using Eq. 2.29.

Circuit simulation is therefore most useful for initial synthesis and component optimization, while electromagnetic simulation is needed for structures whose behavior is determined by distributed fields and layout geometry. Comparing ideal, finite-Q, circuit-parasitic, and EM-based models provides a way to determine which non-idealities dominate the final response.

2.8 Expected influence on measured filter performance

Table 2.1 summarizes the main theoretical relationships that are used later when interpreting the simulated and measured filter responses.

Table 2.1: First-order influence of important non-ideal parameters on the tunable filter.

Parameter	Primary circuit effect	Expected filter-level consequence
$R_{\text{on}} \uparrow$	Increased series dissipation in an active tuning branch	Lower resonator Q, increased passband insertion loss, changed resonance damping, and possible change in S_{11}.
$C_{\text{off}} \uparrow$	Increased RF loading from inactive branches	Lower high-state resonant frequencies, reduced tuning range, stronger interaction between switch states, and potentially reduced isolation.
$C_{\text{PCB}} \uparrow$	Increased effective shunt capacitance	Downward center-frequency shift and changed tuning-step size; matching minima in S_{11} also shift.
Passive-component Q↓	Increased ESR and dissipation	Increased insertion loss and reduced selectivity, especially for narrow fractional bandwidth.
$L_{\text{par}} \uparrow$	Additional series reactance and possible LC self-resonances	Frequency shift, modified inverter coupling, and possible unintended resonant features.
Resonator-node impedance↑	Larger RF voltage for a given power	Increased voltage stress across capacitors and off-state switches.
Temperature↑	Bias- and temperature-dependent switch resistance/capacitance	Power-dependent loss, detuning, and discrepancy between small-signal model and high-power measurement.

The important point is that the switch parameters, passive-component Q, and PCB parasitics are not independent corrections added after ideal filter synthesis. They modify the resonator impedance, stored energy, damping, and coupling that define the filter response itself. The measured S_{21}, S_{11}, center frequency, bandwidth, tuning range, and power handling should therefore be interpreted as consequences of the complete resonator and switch network rather than of the ideal LC values alone.

3

Methods

3.1 Pre-study and Requirement Definition

The first stage of the work was to investigate existing tunable RF filters in order to define realistic design targets and identify suitable filter topologies. Netcom's 5588-3 tunable filter was used as a primary reference, since its published performance was representative of the intended application [15].

From the reported shape factor, defined using the 30 dB and 3 dB bandwidths, the minimum required filter order was estimated to be second order. A first-order filter cannot provide the required roll-off for the specified shape factor [3]. Using the reported insertion loss of approximately 4.1 dB at 5 % fractional bandwidth, the required total filter Q-factor was estimated using Eq. 2.16. This resulted in an approximate target Q-factor of 51. Another way to characterize the shape factor is by the attenuation at a specified offset from the center frequency. A design goal of 22 dB rejection at ±12 % of the center frequency was used, which is representative of commercial off-the-shelf filters of this type.

To understand the relationship between filter order, insertion loss, roll-off, and shape factor, several idealized band-pass filters were simulated in Keysight ADS. These initial simulations used ideal components and were intended to verify the theoretical filter behavior before introducing practical limitations.

Theoretical low-pass prototype filters were transformed into band-pass structures using J-inverters. Both fractional-bandwidth and absolute-bandwidth approaches were investigated. An absolute-bandwidth filter based on the method described in [22] was reconstructed using filter equations from Hong and Lancaster [3]. Component and inverter values were then varied to study their effect on bandwidth, center frequency, and impedance matching.

The switch behavior was initially represented using an engineering model of the Tagore TS63430D GaN switch. This model was used throughout the early design and reverse-engineering stages in combination with ideal passive components.

3.2 Filter Topology Selection

To minimize insertion loss and physical size, the lowest filter order capable of meeting the target specifications was selected. A second-order topology was therefore chosen.

Several filter types were evaluated theoretically using low-pass prototype values from standard filter synthesis equations [3]. A Chebyshev response with approximately 1 dB passband ripple was selected as a compromise between selectivity, insertion loss, and input/output matching. This choice provided sharper roll-off than a Butterworth response while maintaining acceptable voltage standing wave ratio performance.

The selected topology consisted of two resonant sections connected using three admittance inverters, designed around the center frequency for the band using Eq. 2.1. This structure was chosen because J-inverters allow practical band-pass implementations using parallel resonators, reducing the need for series resonant paths with high parasitic resistance.

3.3 Circuit Design and Optimization

The initial circuit design was performed in Keysight ADS. Component values were first calculated analytically from the selected low-pass prototype and then refined using numerical optimization. Two switching architectures for the switch itself were investigated. The first used binary-weighted internal capacitances, while the second used the lowest possible capacitance for each switch. The binary-weighted architecture offered more flexible tuning, but introduced increased parasitic loading and reduced the achievable Q-factor. The fixed-value switching architecture was therefore selected for the final design.

The first optimization stage used ideal passive components together with the engineering model of the GaN switch. The filter was optimized across all switching states simultaneously. The optimization goals included center frequency accuracy, fractional bandwidth, insertion loss, reflection coefficient, and shape factor. The optimization targets are summarized in Table 3.1.

Table 3.1: Optimization goals used during filter design.

Goal	**States**	**Target value**	**Weight**
Center frequency, S_{21}	0	520 MHz $\pm$ 1 MHz	2
Center frequency, S_{21}	255	225 MHz $\pm$ 1 MHz	2
Fractional bandwidth	All	0.05	4
Average insertion loss, S_{21}	All	$<$ 4.1 dB	1
Minimum reflection coefficient, S_{11}	All	< -10 dB	1
S_{11} bandwidth	All	15 MHz	1
Shape factor, BW_{30}/BW_3	All	$<$ 6	2

Initial optimization was performed using the Gradient MinMax algorithm in ADS.

The results were then refined using the Hybrid optimizer to improve convergence and avoid local minima. The optimization process was repeated after each major modeling improvement.

3.4 Transition to Real Component Models

After the ideal-component design had been established, the passive components were replaced with finite-Q component models. The Q-values were estimated by matching practical component values to the INDQ2 and CAPQ models in Keysight ADS.

Components from the Coilcraft SQ1515 inductor series and Kyocera AVX Accu-P capacitor series were selected, since they were commercially available and suitable for the intended frequency range. This modeling step was used to bridge the gap between ideal components and measured component data.

The final simulation stage used measured component models on Rogers RO4350D substrate. This transition significantly changed the filter behavior, especially for the inductors. The measured inductor models included substrate-dependent parasitic effects that were not present in the ideal or free-space component models. These parasitics shifted the resonant frequencies and broadened the filter passbands, particularly at higher frequencies.

Because of these effects, several previously optimized component combinations became impractical. The filter topology was therefore adjusted using the available measured component library. Additional capacitive compensation was introduced to reduce excessive bandwidth broadening and improve agreement with the target response.

3.5 Electromagnetic Simulation

To improve the accuracy of the circuit model, electromagnetic simulations were performed for the PCB structures surrounding the switch nodes. These simulations were used to estimate parasitic capacitance, inductance, and impedance deviations introduced by the physical layout. Both Keysight ADS Momentum Microwave and FEM simulations were used. One side of the filter was simulated without passive or active components populated, and all ports were referenced to $50\,\Omega$. The substrate stack-up comprised a $35\,\mu\text{m}$ copper layer on a 20 mil Rogers RO4350D substrate with $\epsilon_r = 3.66$, followed by a second $35\,\mu\text{m}$ copper layer.

The EM simulations showed that the switch-node geometry and grounding structure introduced additional capacitance. This had a measurable effect on the filter response and was therefore included in later tuning stages. Some impedance deviation was also observed, although the dominant effect was the added parasitic capacitance.

A transmission line structure was also simulated and compared with measurements from the Tagore evaluation board. This comparison was used to evaluate the accuracy of the substrate and transmission-line models before applying them to the complete filter design.

3.6 PCB Fabrication and Assembly

The PCB was fabricated on Rogers RO4350D substrate with a thickness of 20 mil. Assembly was performed partly in the MC2 assembly laboratory and mainly in the ETA student laboratory.

Solder paste was first applied using a stencil, after which the board was assembled using reflow soldering. The SMA connectors and DC control pins were manually soldered after reflow. The assembled board was visually inspected before electrical testing. Several assembly and bring-up issues were encountered before reliable testing could be performed; these are described in Section 3.10.

3.7 Measurement Automation

Measurement automation was developed to improve repeatability and reduce measurement time across the large number of switching states.

An initial switch controller was constructed using a Raspberry Pi Pico and transistor driver stages to control the GaN switches on the evaluation board. Since the required switch control current was very small, the transistor stages were later removed and the Pico was connected directly to the switch control interface. A USB-based control protocol was developed to set the switch states automatically.

Automation software was also developed for controlling the vector network analyzers. An HP 8753C VNA was first used to test the automation through GPIB communication. Later measurements were performed using an R&S ZND vector network analyzer. Since this instrument communicated using a socket-based protocol, Touchstone files were generated on the control computer rather than transferred directly from the VNA.

Using the automated setup, multiple switch states could be measured sequentially without manual reconfiguration.

3.8 Measurements

Measurements were first performed on the Tagore evaluation board, which contained the GaN switch and a transmission line structure. The purpose of these measurements was to compare the switch behavior with the supplied simulation model and to evaluate the transmission-line model.

The evaluation board was tested under several operating conditions, including operation with the internal charge pump enabled and disabled, with and without switch supply voltage, and across multiple switch states. Measurements were performed using a calibrated R&S ZND vector network analyzer.

The completed filter was tested progressively to reduce the risk of damaging the circuit. The measurement procedure consisted of:

1. Visual inspection of solder joints and component placement.
2. DC bring-up to verify current consumption and control functionality.
3. Low-power RF testing at $-10\,\mathrm{dBm}$.
4. Verification of the switching mechanism across all states.
5. Frequency-response measurements using a calibrated VNA.
6. Incremental power testing while monitoring thermal behavior.

After low-power testing, a power sweep was first performed using only the VNA at output powers of $-20\,\mathrm{dBm}$, $-10\,\mathrm{dBm}$, $0\,\mathrm{dBm}$, and $6\,\mathrm{dBm}$. A second sweep was then performed with an RF amplifier before the PCB and attenuation after the PCB, giving estimated input powers at the filter of up to $20\,\mathrm{dBm}$. A third sweep extended the estimated filter input power to approximately $30\,\mathrm{dBm}$ to determine whether the response characteristics changed with increasing RF power.

3.9 Measurement Equipment

The main measurement equipment used in the project is listed in Table 3.2.

Table 3.2: Measurement equipment used during the project.

Equipment	Model
Vector network analyzer	HP 8753C
Vector network analyzer	R&S ZND
Switch controller	Raspberry Pi Pico H
Signal generator	R&S SMC100A
Spectrum analyzer	R&S FSL

3.10 Prototype Troubleshooting and Fault Isolation

The fabricated prototype did not initially behave as predicted by simulation. Troubleshooting was therefore incorporated into the experimental method as an iterative fault-isolation procedure. The purpose was to separate switch-related effects from faults or non-idealities in the passive filter network, PCB layout, grounding, and assembly. At each stage, the hardware configuration was simplified where necessary, the resulting RF response was measured, and the observations were compared with corresponding circuit simulations. This procedure also established which hardware configuration could be used for the subsequent prototype measurements.

3.10.1 Switch Failures and Current Consumption

The first measurements of the completed filter showed significantly lower transmission than expected, although a passband was present. During subsequent testing several switches failed and became permanently shorted, as shown in Fig. 3.1. During the repair process an RF trace was damaged, making the construction of a second board necessary.

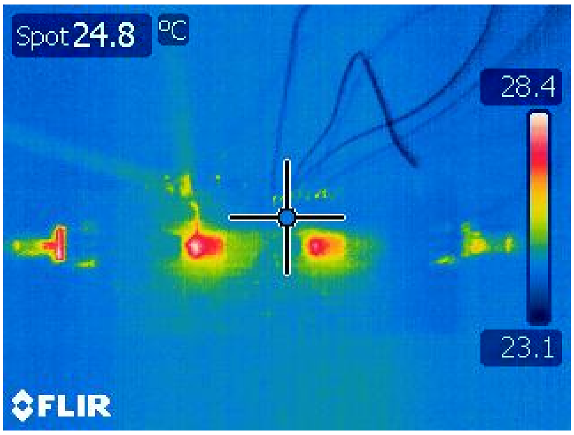

Figure 3.1: Board with broken switches.

An early indication that the hardware was malfunctioning was the supply current. The first board drew approximately 1380 µA. Initially this was considered acceptable because the switch datasheet was interpreted as specifying a current consumption of approximately 220 µA for six switches and 50 µA for two switches, giving an expected current draw of approximately 1420 µA.

Later investigation indicated that the expected current consumption was approximately 50 µA per switch, using the TS85410L datasheet as a consistency check. For eight switches this corresponds to approximately 400 µA. The measured current was therefore significantly higher than expected and should have been treated as an indication of a fault condition.

The replacement board drew between 350 µA and 1300 µA, depending on the amount of rework performed. Since repeated failures occurred at the same switch locations, the problem was unlikely to be caused solely by random soldering defects. The repeated location dependence suggested either a layout-related discontinuity or a mechanical sensitivity that made those positions more susceptible to poor solder joints.

A plausible contributing factor identified later was the missing RF ground connection, which altered the RF return path and may have increased voltage stress at the switch nodes.

3.10.2 Isolation of the Switch Network

As additional switches failed, testing continued using only four switches. The measured response still exhibited poor transmission and multiple resonant peaks. To determine whether the switching network was responsible, the filter switches were removed while leaving the input switches in place.

The resulting response is shown in Fig. 3.2. The measured transmission was approximately -19 dB and exhibited three resonant peaks rather than the single passband predicted by simulation.

Figure 3.2: Filter response with the filter switches removed and only the input switches connected.

Since the response remained poor, the remaining switches were removed and replaced with direct wire connections. During this process a signal pad was damaged, preventing a short repair. Instead a replacement wire approximately 12 mm long was installed, as shown in Fig. 3.3.

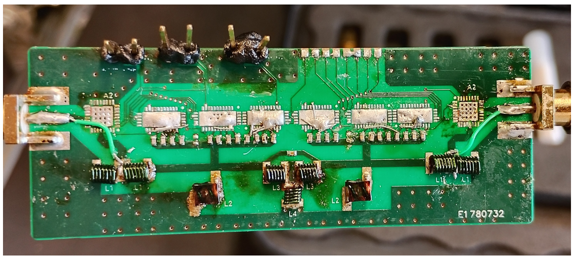

Figure 3.3: Board with all switches removed.

The replacement wire corresponds to approximately $\lambda/20$ at 660 MHz and was therefore considered electrically short for the purpose of troubleshooting measurements.

Measurements performed with all switches removed are summarized in Table 3.3.

Table 3.3: Measured resonant-response values with all switches removed. Complete S_{11} data were not available for every state.

State	S_{11} (dB)	$f(S_{11})$ (MHz)	S_{21} (dB)	$f(S_{21})$ (MHz)
0	-7.872	796	-5.1	788
128			-13.4	257
255			-12.2	210

The response still deviated significantly from simulation. During this stage two additional switches failed during repeated soldering operations.

3.10.3 Grounding Investigation

Testing then continued using only two verified switches. Particular care was taken to ensure that the substrate was not bent and that all connections were intact before measurements were performed.

The resulting response is shown in Fig. 3.4. The insertion loss appeared reasonable, but the expected frequency shift between states was largely absent.

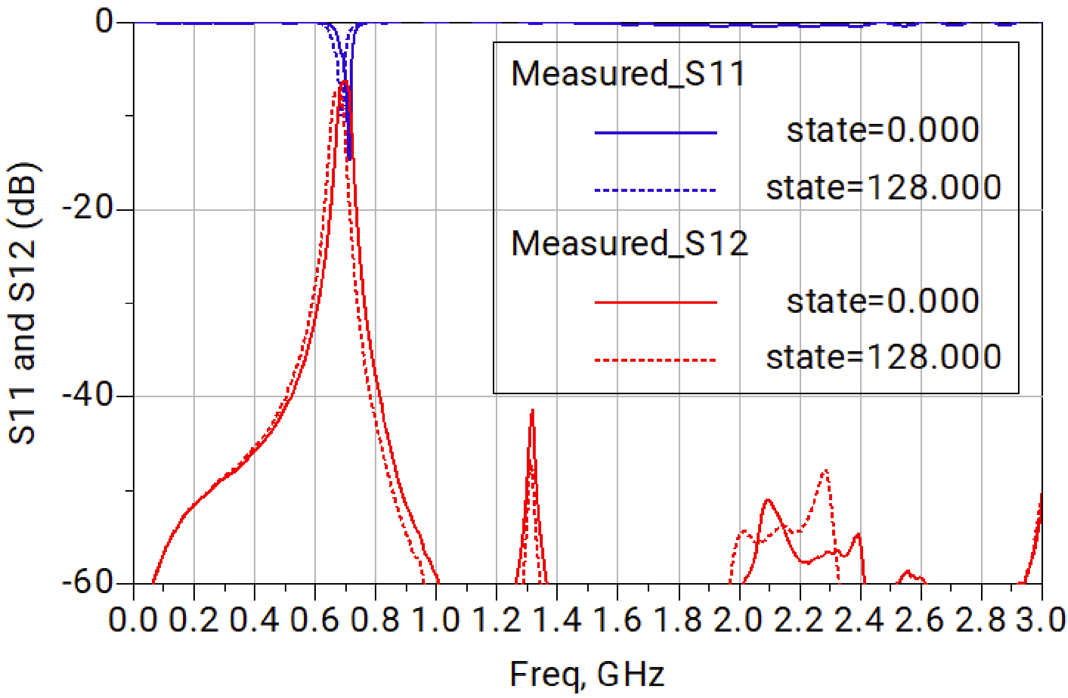

Figure 3.4: Measured filter response before the grounding issue was identified.

Further investigation revealed that the RF output grounding had not been connected correctly in the PCB design. Although the filter was developed as a largely modular structure, the RF return path for the filter switches was not completed in the final layout. The missing connection therefore had to be added manually during troubleshooting.

The missing connection was repaired by soldering a wire across the output ground pads. Ground continuity was verified using continuity measurements from the switch-side capacitor pads to ground.

3.10.4 Comparison with Simulation

After the grounding issue was corrected, new measurements were performed. The measured response appeared considerably more reasonable and qualitatively resembled the simulated filter response.

The comparison between simulation and measurement is shown in Fig. 3.5.

Two power sweeps were subsequently performed. The first ranged from −20 dBm

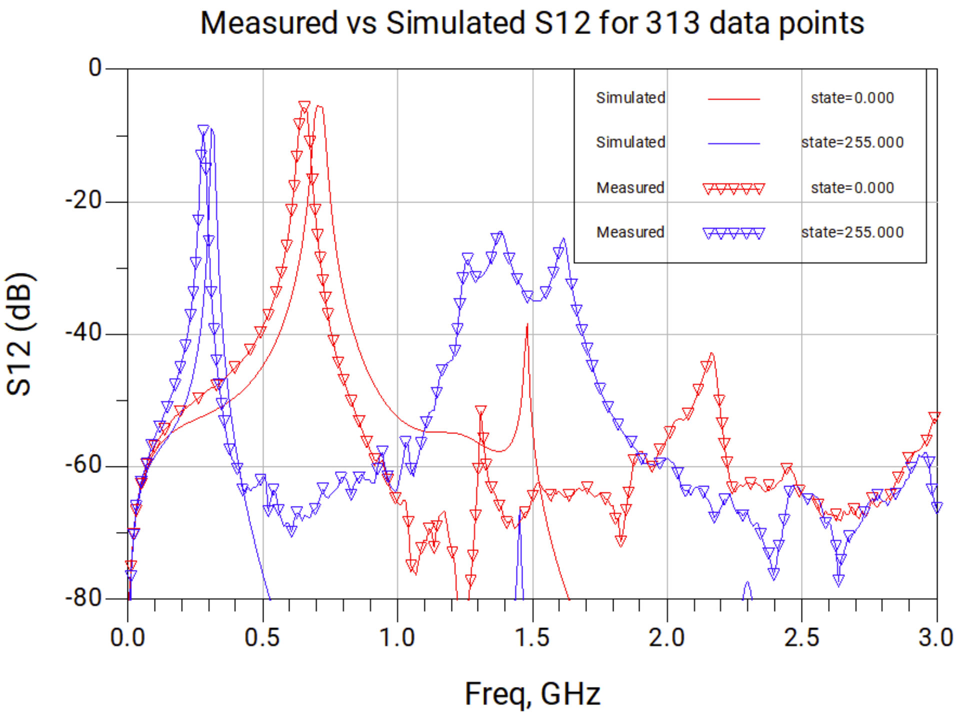

Figure 3.5: Simulated response, shown in red, and measured filter response, shown in blue. The measurement span was 100 kHz to 3 GHz with 313 frequency points.

to 6 dBm. The second used an amplifier followed by attenuation and exposed the filter to approximately 20 dBm of RF power.

Although the low-resolution measurement appeared encouraging, more detailed measurements were considered necessary.

3.10.5 High-Resolution Measurements and Fault Modeling

A higher-resolution measurement was performed from 100 kHz to 1 GHz using 5001 frequency points. Figure 3.6 compares the simulation, the initial low-resolution measurement, and the high-resolution measurement.

The high-resolution data differed significantly from both the simulation and the earlier measurement. This suggested that additional faults or parasitic effects were present.

Visual inspection suggested that capacitor C4 had accidentally been shorted to ground during soldering rework performed after the coarse measurement. This fault was introduced into the ADS model and reproduced the dual resonance observed in the upper passband. Additional modifications were then made by removing one C8 capacitor and introducing additional capacitances to the capacitor bank path. Initial capacitance estimates were derived from the evaluation-board measurements and subsequently adjusted to improve agreement with the measured prototype response. This should therefore be interpreted as a fitted diagnostic fault model rather than an independent extraction of the physical parasitic capacitances.

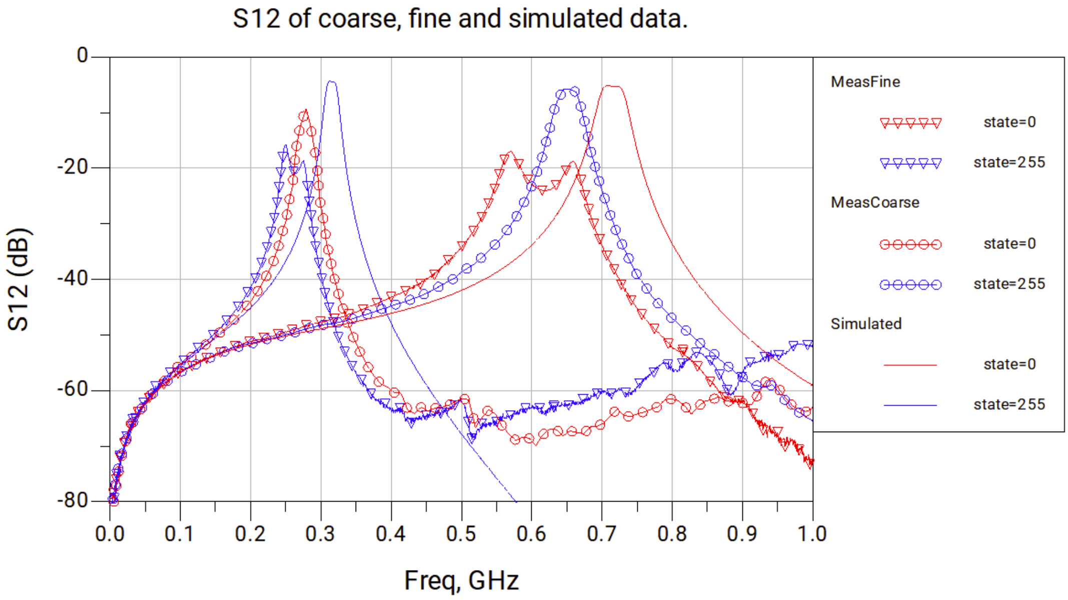

Figure 3.6: Comparison of the simulated response (unmarked curves), the low-resolution measurement (circular markers), and the high-resolution measurement (triangular markers) for the pass-through configuration.

Including these modifications produced significantly better agreement between simulation and measurement, as shown in Fig. 3.7.

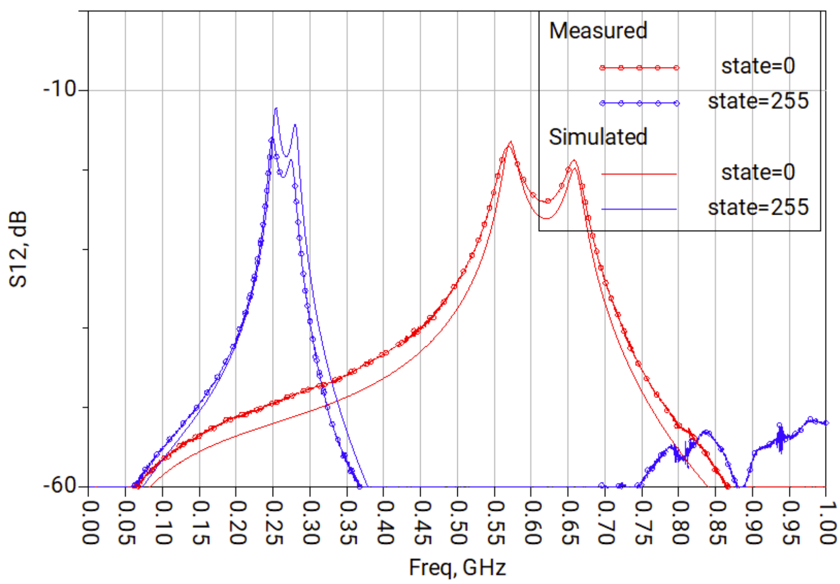

Figure 3.7: Comparison between the modified simulation (unmarked curves) and measured response (marked curves) after introducing the C4 fault and asymmetric C8 capacitances. Blue and red correspond to the two measured switch states.

The results suggest that the discrepancy between simulation and hardware was caused by a combination of missing RF grounding, reduction of switches used, and additional parasitic capacitances introduced during rework.

After the C4 short circuit was corrected, the measured response still indicated additional discrepancies. The C8 capacitors were therefore replaced with the closest available value, 10 pF, using components from a different manufacturer. With the switch enabled, the resulting response showed poor matching, while with the switch disabled the resonant frequency was outside the intended tuning range. The C5–C7 branches were subsequently shorted to ground to further simplify the circuit. Figures 3.8 and 3.9 compare this configuration with the corresponding simulation. In the fitted model, the added capacitance was approximately 19.5 pF for the lower-frequency state and 6.5 pF for the higher-frequency state. The physical origin of this effective capacitance was not independently verified but probably includes contributions from the switch and, to a lesser extent, layout parasitics.

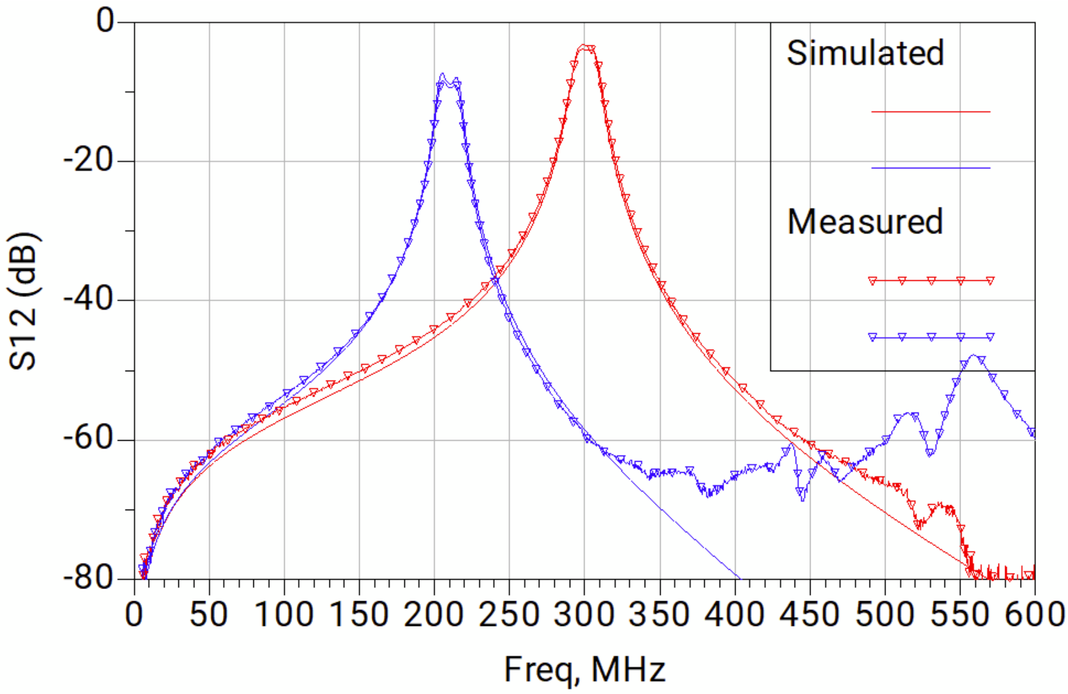

Figure 3.8: Simulated S_{12} response with added capacitance and one switch position removed.

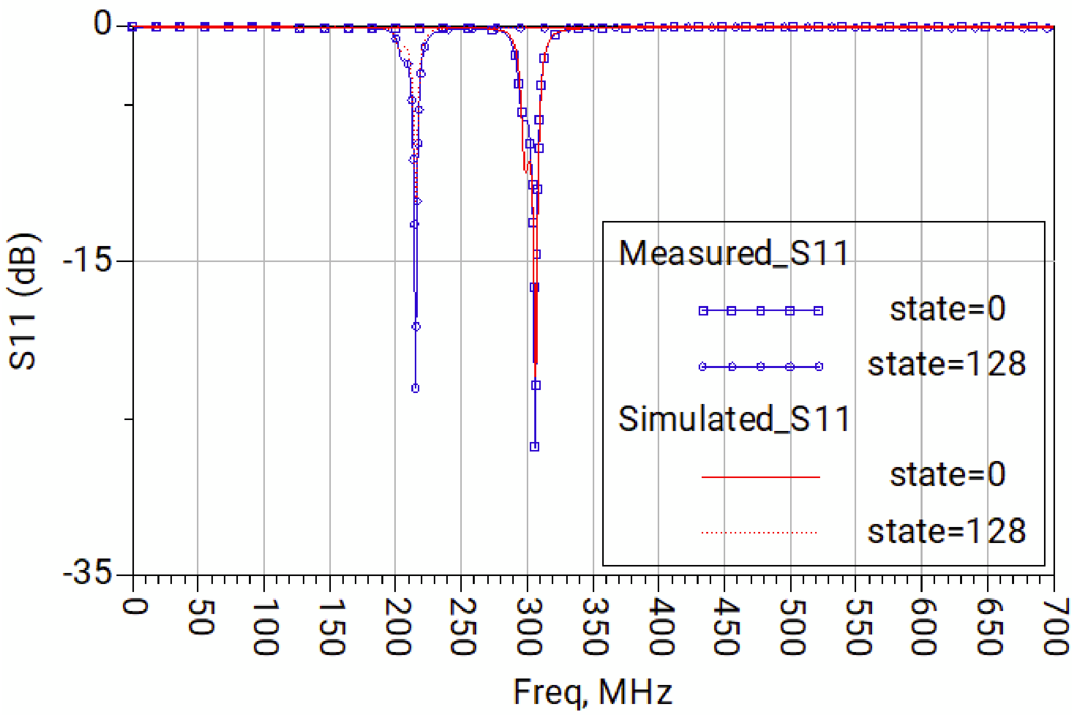

Figure 3.9: Simulated S_{11} response with added capacitance and one switch position removed.

4 Results

This chapter presents the experimental and simulated results obtained during the project. The results are divided into three parts. First, measurements of the supplied GaN switch evaluation board are presented and compared with the provided engineering model. Second, the simulated performance of the complete filter bank is shown using real component models and electromagnetic simulation of the critical PCB structures. Finally, measurements of the fabricated prototype are presented.

The measured prototype results should be interpreted with care. During assembly and troubleshooting, several switches failed and parts of the circuit were reworked. The final measured configuration therefore did not correspond exactly to the originally simulated complete filter bank. The prototype measurements are consequently used mainly to evaluate resonant behavior, frequency shift, parasitic effects, and power-related changes rather than to demonstrate full compliance with all original filter-bank specifications.

4.1 Evaluation Board Measurements

A GaN switch evaluation board was provided by the manufacturer. The board was matched to $50\,\Omega$ and included control pins for setting the switch states. These measurements were performed to compare the measured switch behavior with the supplied engineering model before using the model in the complete filter simulation.

The measured transmission, S_{12}, with the switch supply voltage disconnected followed the same general trend as the engineering model, although deviations were visible at higher frequencies. Fig. 4.1 shows the corresponding response when the supply voltage was disconnected. These measurements were used to verify the expected switch behavior and to identify differences between the physical switch and the model used in ADS.

The evaluation board also included a $50\,\mathrm{mm}$ long $50\,\Omega$ transmission line. Since a similar transmission-line structure was used in the final design, this structure was measured and compared with a microstrip-line simulation in ADS. The measured and simulated S_{12} responses are shown in Fig. 4.2. The measured and simulated S_{11} responses are shown in Fig. 4.3.

The transmission measurement showed good agreement in insertion loss and general frequency dependence. The reflection response showed larger differences, indicating

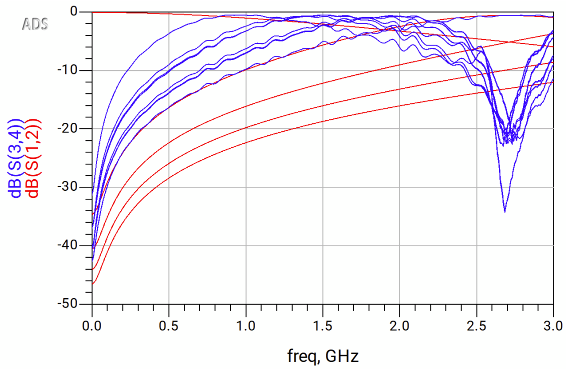

Figure 4.1: Measured S_{12} response of the evaluation board with VDD disconnected, compared with the supplied engineering model.

that the substrate model and line geometry captured the main behavior but did not fully reproduce all impedance discontinuities and parasitic effects present on the physical board. These results motivated the later use of EM simulation for the critical switch-node structures.

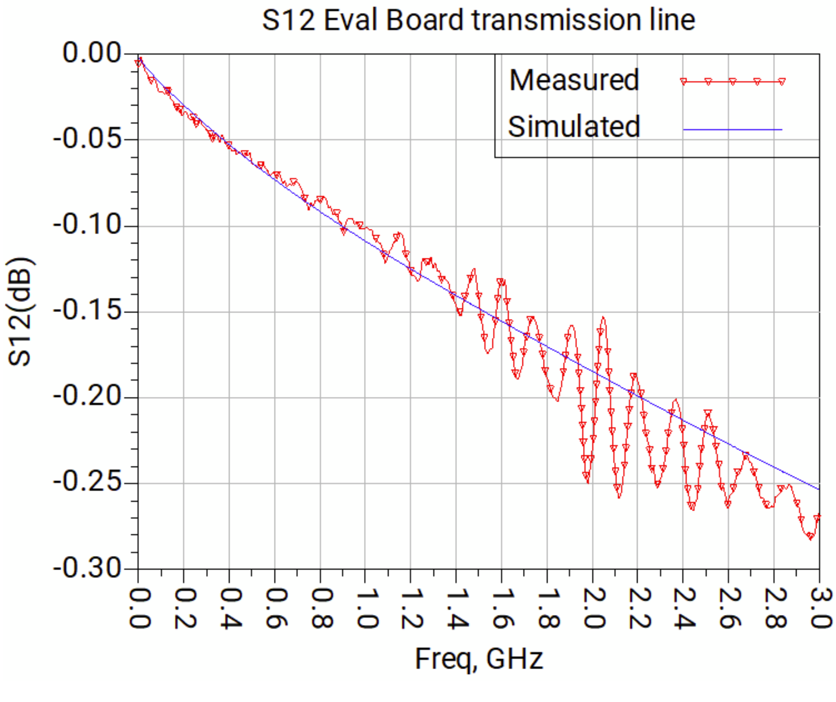

Figure 4.2: Measured S_{12} response of the 50 mm evaluation-board transmission line, shown in blue, compared with the ADS microstrip simulation, shown in black.

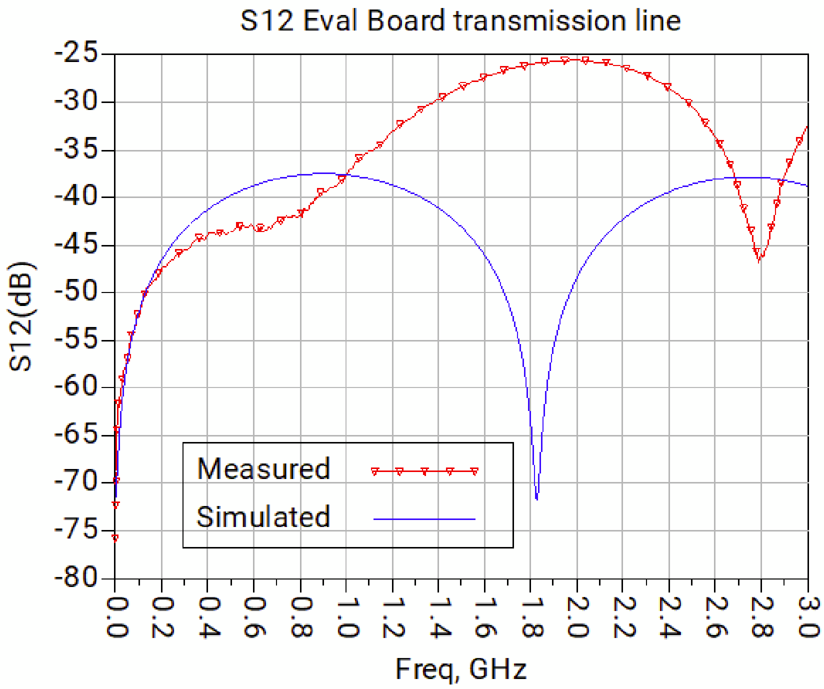

Figure 4.3: Measured S_{11} response of the 50 mm evaluation-board transmission line, shown in blue, compared with the ADS microstrip simulation, shown in red.

4.2 Simulated Filter Performance

The final full-filter simulations used real passive component models together with EM-simulated switch-node structures. The passive components were modelled using Modelithics models on Rogers RO4350D substrate where available. The component values and simulation models used in the final simulated design are listed in Table 4.1. The corresponding PCB layout is shown in Fig. 4.4, including the complete layout, the capacitor-bank region, and the switch-node structure used for EM simulation.

Fig. 4.5 shows the simulated S_{21} response for all switching states of the filter bank. The simulated responses cover approximately the intended 225 MHz to 520 MHz frequency range with 256 states with binary ladder capacitances. The passbands shift across the tuning range as the switched capacitance states are changed. The simulated insertion loss varies between states, which is expected because the component Q-factors, switch parasitics, and effective resonator loading are not constant across the full frequency range.

The simulated high-side and low-side rejection are shown in Fig. 4.6. The rejection remains within the intended range for most simulated states, although the low-side and high-side rejection are not symmetric over the full tuning range. This asymmetry is caused by the changing resonator values, finite component Q, and the non-ideal impedance of the switch-node structures.

Fig. 4.7 shows the simulated system loss and fractional bandwidth for the different

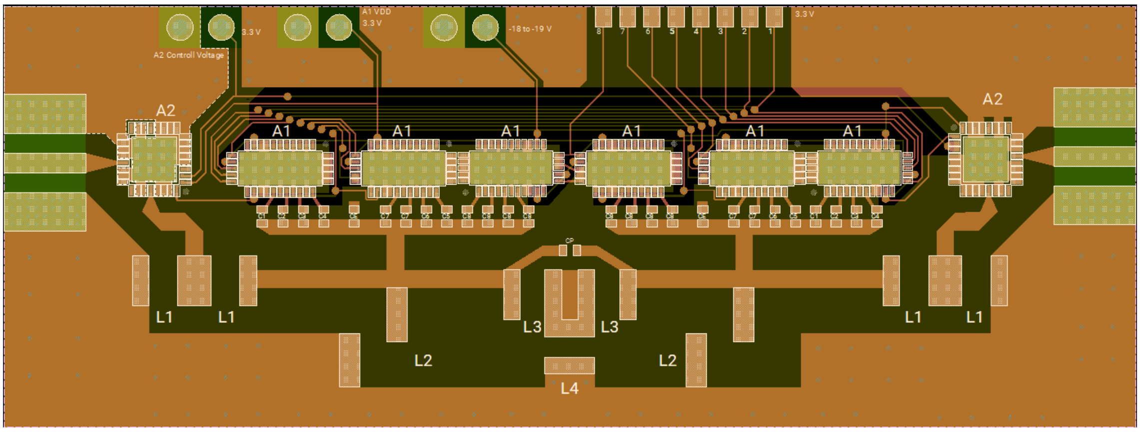

(a) Complete PCB layout.

(b) Detailed view of the capacitor-bank structure.

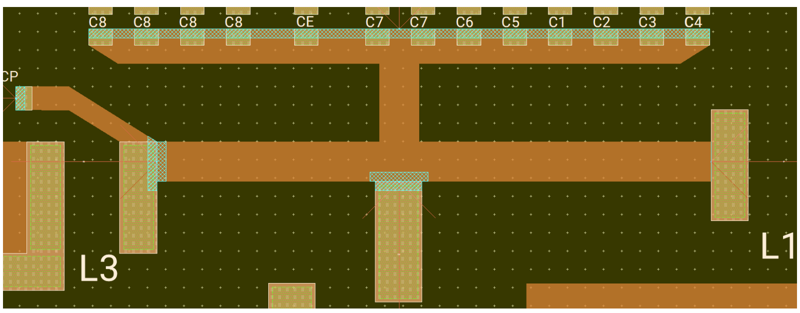

(c) Switch-node region used for EM simulation, with equal reference impedances assumed at the C_p, L3, L1, capacitor-bank, and L2 ports.

Figure 4.4: PCB layout and detailed views of critical filter structures.

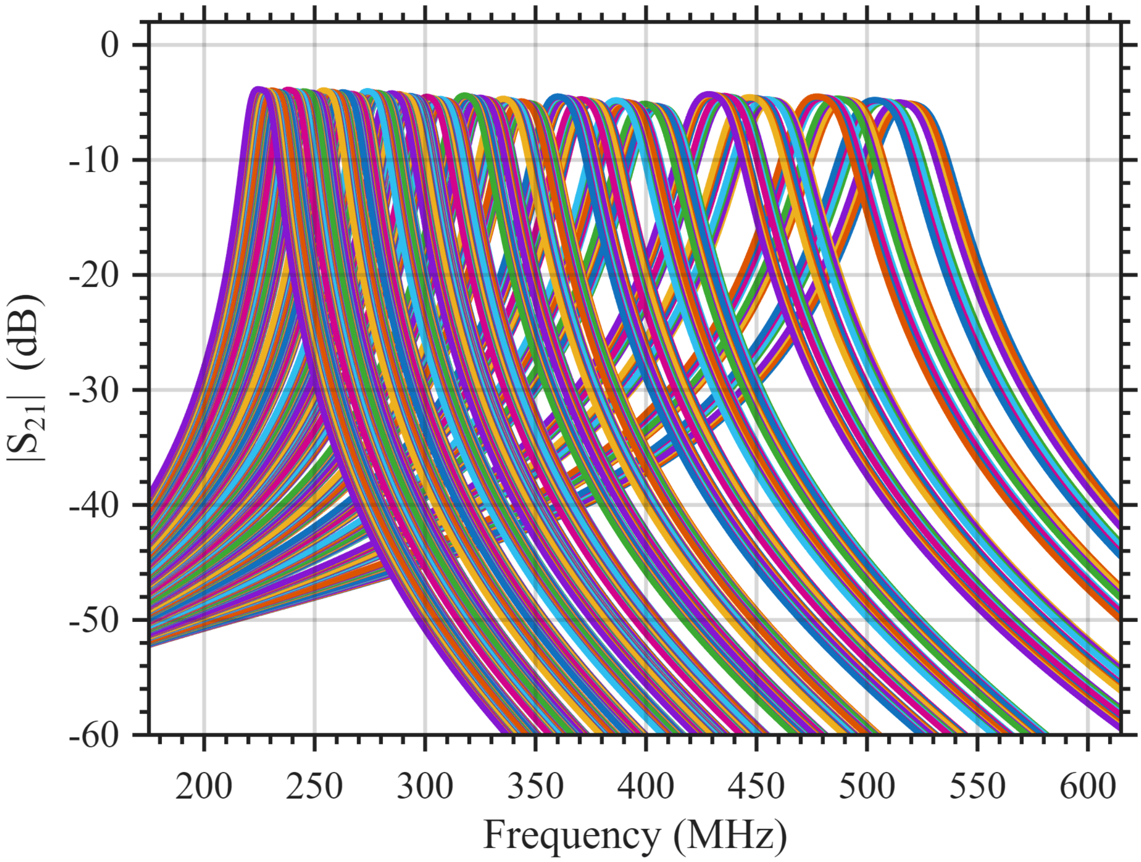

Figure 4.5: Simulated S_{21} response for all switching states of the complete filter bank using real component models and EM-simulated switch-node structures.

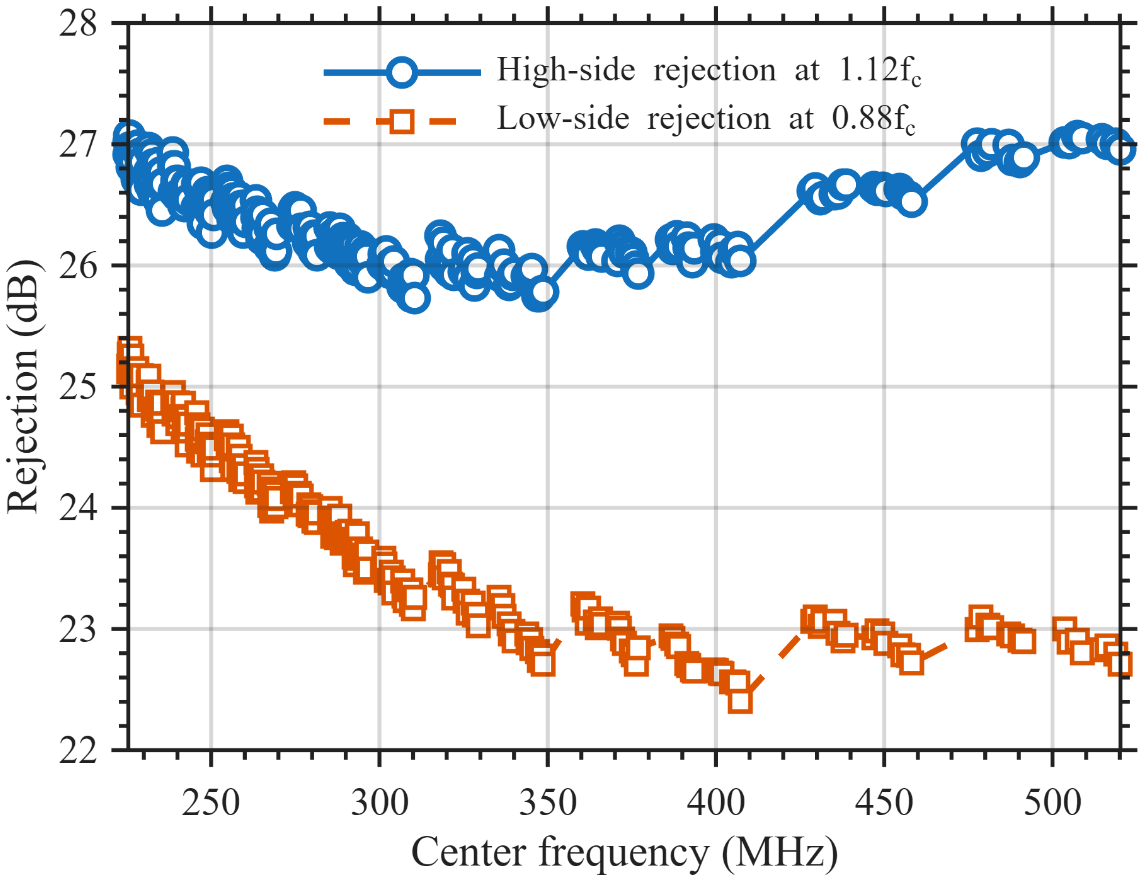

Figure 4.6: Simulated high-side and low-side rejection for the filter-bank states.

Table 4.1: Components and simulation models used in the final filter simulation. Passive components were modelled using Modelithics models on Rogers RO4350D substrate where available.

Position	Component Value	Simulation Model
L1	47 nH	Coilcraft 11SQ47N
L2	5 nH	Coilcraft A02Mini
L3	33 nH	Coilcraft 11SQ33N
L4	27 nH	Coilcraft 11SQ27N
C1	0.3 pF	Kyocera AVX ACCU-P 0402
C2	0.6 pF	Kyocera AVX ACCU-P 0402
C3	1.2 pF	Kyocera AVX ACCU-P 0402
C4	2.5 pF	Kyocera AVX ACCU-P 0402
C5	5.1 pF	Kyocera AVX ACCU-P 0402
C6	10 pF	Kyocera AVX ACCU-P 0402
C7	10 pF	Kyocera AVX ACCU-P 0402
C8	9.1 pF	Kyocera AVX ACCU-P 0402
Cp	0.2 pF	Kyocera AVX ACCU-P 0402
CE	Empty	
A1	TS63430D	Engineering model for TS63430D
A2	TS85410L	Engineering model for TS63430D*

* No model for TS85410L was available during testing.

switching states. The fractional bandwidth remains close to the target value of approximately 5 %, ranging from 4.9 % to 5.3 %, while the loss varies with frequency and switch state. The simulated loss is lowest in parts of the tuning range and increases for other states, mainly due to component losses and non-ideal resonator loading.

The EM simulation of the switch-node structure indicated an impedance of approximately 200 Ω at the capacitor-bank ports shown in Fig. 4.4c. The simulated impedance is shown in Fig. 4.8. This impedance is significantly higher than the 50 Ω system impedance. The high switch-node impedance is important for two reasons. First, it affects the tuning and matching of the filter. Second, it increases the RF voltage stress across the switched capacitors for a given input power, which later became a relevant limitation during power testing.

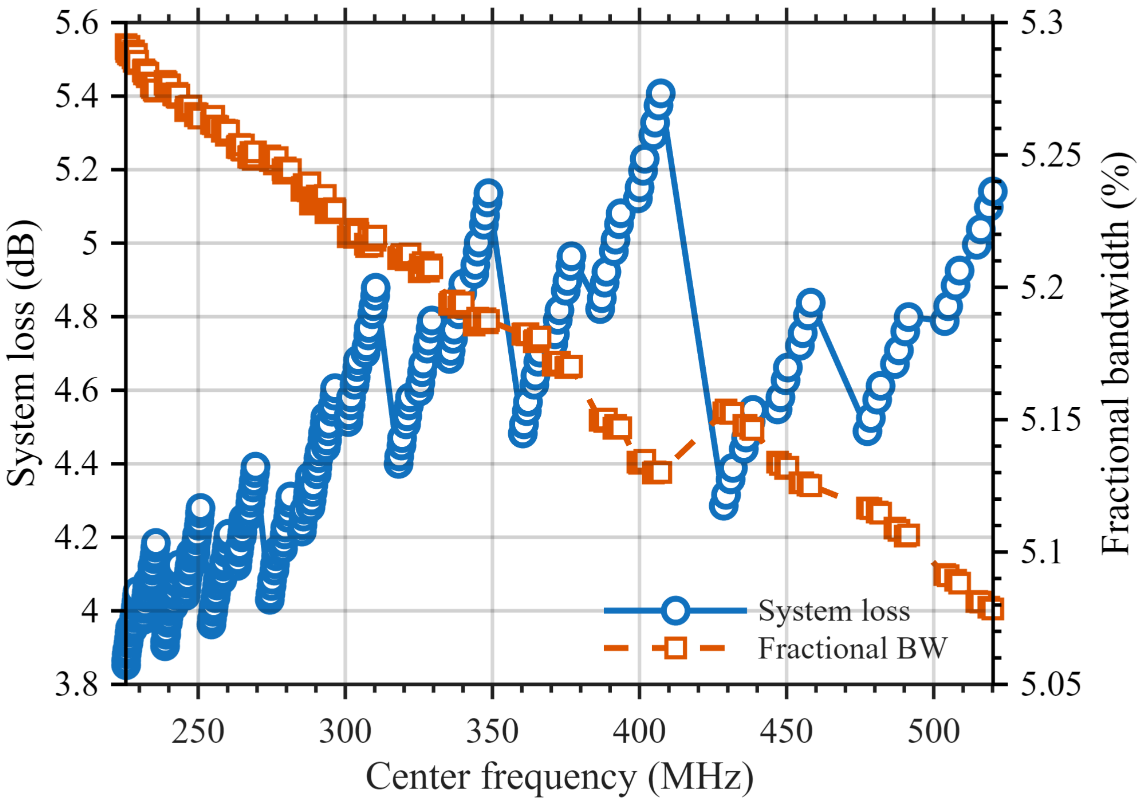

Figure 4.7: Simulated insertion loss and fractional bandwidth for the filter-bank states.

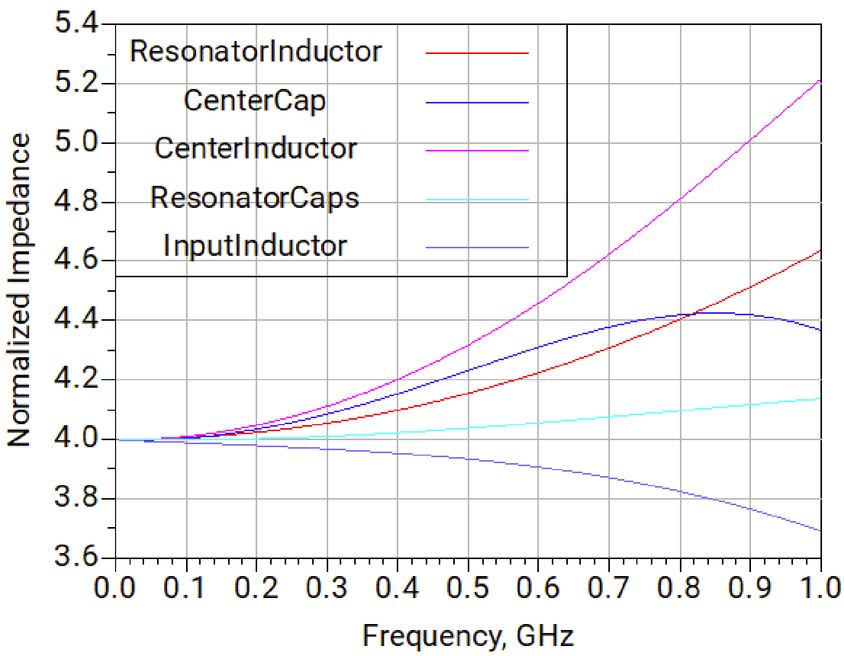

Figure 4.8: EM-simulated impedance magnitude at the input ports of the switch-node structure shown in Fig. 4.4c, normalized to 50 Ω.

4.3 Prototype Measurements

The fabricated prototype was measured after troubleshooting and partial rework. At this stage, only the two switches controlling C8 remained functional, and C7 had been changed from 10 pF to 9.1 pF. During an earlier measurement, one of the switches that subsequently failed had been kept in the off state, shifting the highest-frequency response toward the intended center frequency.

Consequently, the measured hardware no longer represented the complete filter bank used in the original simulations. To enable a more representative comparison, the simulation model was therefore modified to match the measured hardware configuration by disconnecting the remaining switched capacitors and removing the input switches, which had also been damaged during bring-up. The complete list of components used in the measured configuration is given in Table 4.2.

Table 4.2: Components used during filter measurements. Both variants of C8 capacitor shown.

Position	**Component Value**	**Make and Model**
L1	47 nH	Coilcraft 11SQ47N
L2	5 nH	Coilcraft A02Mini
L3	33 nH	Coilcraft 11SQ33N
L4	27 nH	Coilcraft 11SQ27N
C1	0.3 pF	WE-CSRF 0402, 50 V
C2	0.6 pF	WE-CSRF 0402, 50 V
C3	1.2 pF	WE-CSRF 0402, 50 V
C4	2.5 pF	WE-CSRF 0402, 50 V
C5	5.1 pF	WE-CSRF 0402, 50 V
C6	10 pF	WE-CSRF 0402, 50 V
C7	9.1 pF	WE-CSRF 0402, 50 V
C8, coarse	9.1 pF	WE-CSRF 0402, 50 V
C8, fine	10 pF	Murata GCQ1555C1H100JB01D, 50 V
Cp	0.2 pF	WE-CSRF 0402, 50 V
CE	Empty	
A1	TS63430D	Only innermost position populated
A2	Wire	Direct wire connection from SMA to L2

The resulting comparison between measurement and simulation is shown in Fig. 4.9. The measured response showed the same general resonant behavior as the modified simulation, but the resonant frequencies were shifted downward to approximately 90 % of the simulated values. The measured S_{11} response also differed from the simulation, especially in the lower-frequency region, indicating that the physical prototype had additional parasitic effects or faults not included in the first modified model.

An additional measurement was performed with the C5–C7 capacitors shorted to ground and the C8 capacitors replaced by 10 pF components because the 9.1 pF components were no longer available. The comparison with the corresponding simu-

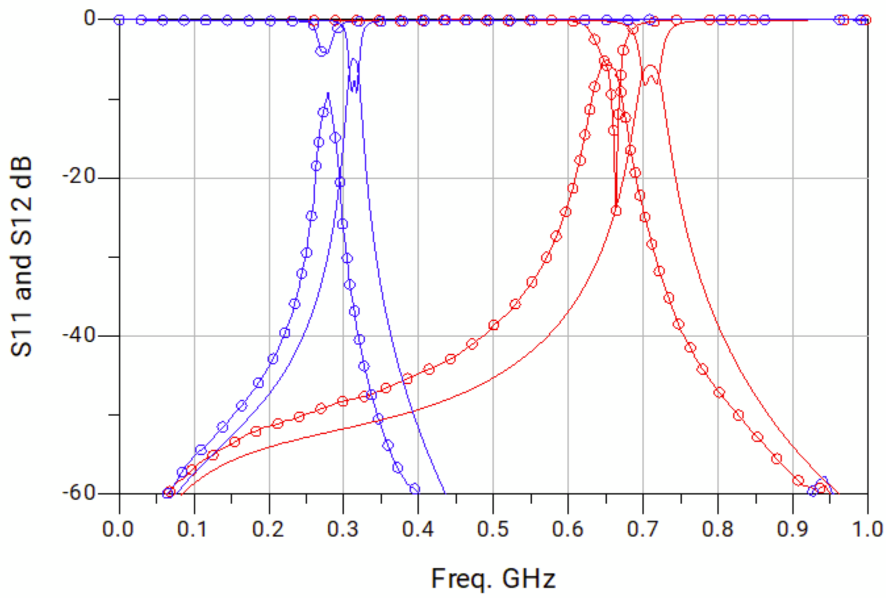

Figure 4.9: Comparison between the coarse measurement of the reworked prototype, shown in blue, and the modified simulation, shown in red. The measured resonances are shifted downward relative to simulation.

lation is shown in Fig. 4.10. The same modified configuration is also compared with the measured response in Figs. 3.8 and 3.9.

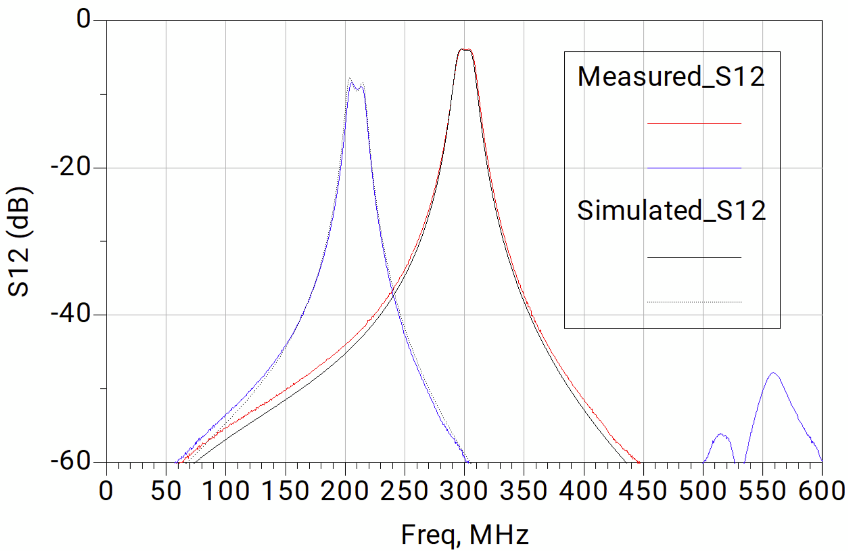

(a) Measured and simulated S_{12} response, with the simulated response shown in black.

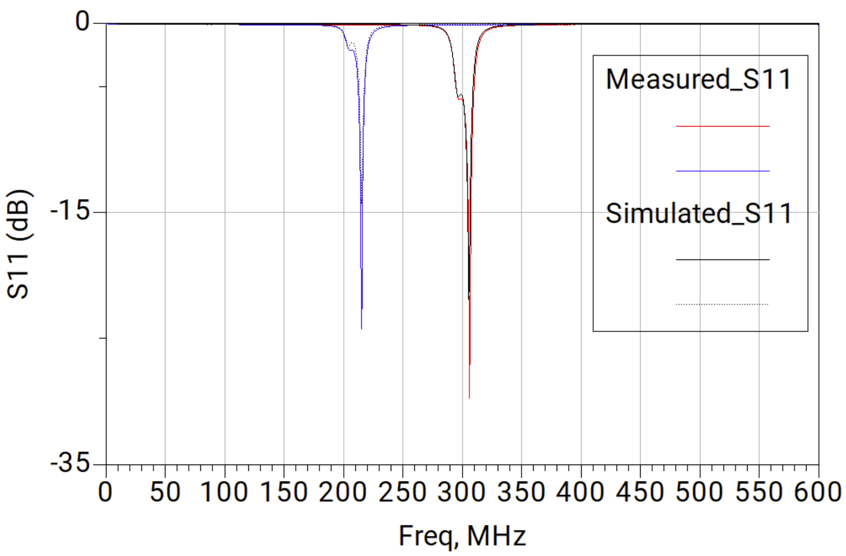

(b) Measured and simulated S_{11} response, with the simulated response shown in black.

Figure 4.10: Comparison of measured and simulated S_{11} and S_{12} with one switch gate in the open state and a 5 % capacitor-value variation included in the simulation.

4.4 Power Sweep Measurements

Power-sweep measurements were performed to investigate whether the response changed with increasing RF input power. The intended RF amplifier was unavailable during the measurement campaign. Power testing was therefore performed using an alternative amplifier with unspecified gain and a specified P_{1dB} of approximately 28 dBm, followed by a 30 dB attenuator. The sweep for the DUT with the switches off is shown in Fig. 4.11. The visible compression is attributed primarily to the amplifier rather than to the DUT.

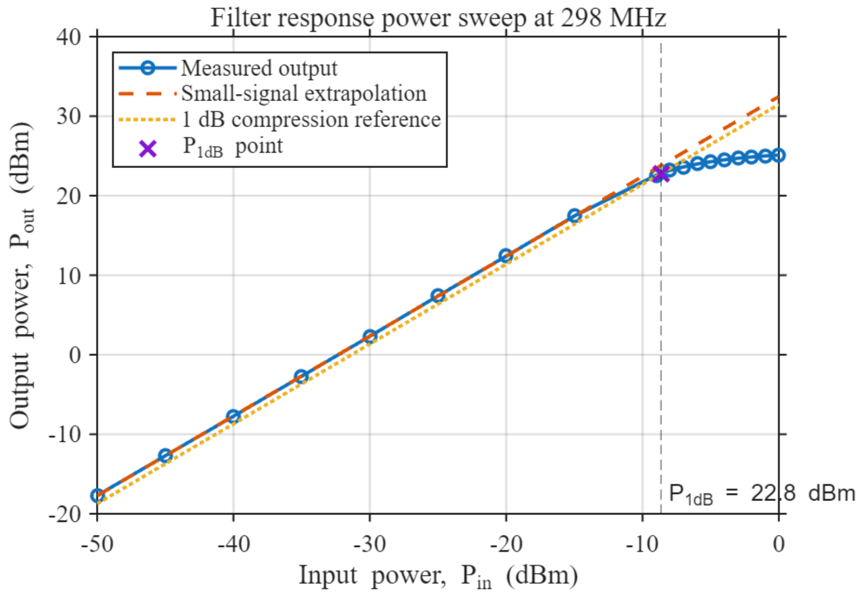

Figure 4.11: Power sweep of the amplifier–filter–attenuator measurement chain for the filter state centered near 298 MHz. The observed compression is dominated by the RF amplifier.

An additional VNA power sweep was performed with the amplifier and attenuator in the measurement chain to investigate whether the filter response changed with increasing input power. The VNA output power was varied from −15 dBm to 5 dBm in 5 dB increments; the resulting responses are shown in Fig. 4.12.

A power-dependent change in the passband response is visible at higher drive levels. However, the measurement cannot be used to determine the intrinsic P_{1dB} of the DUT because compression was also present in the measurement chain.

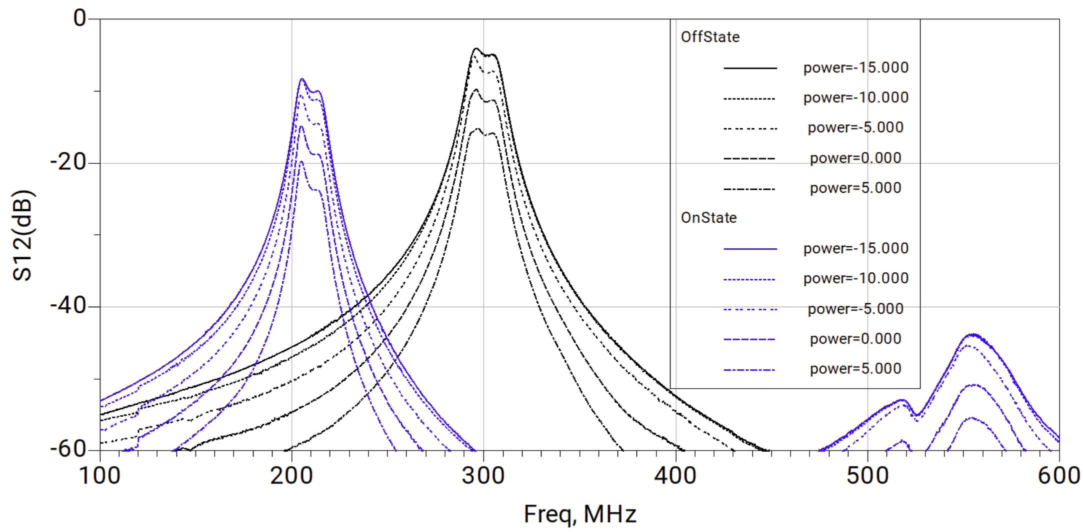

Figure 4.12: VNA power sweep for the two measured switch states, with the VNA output varied from −15 dBm to 5 dBm in 5 dB increments. A power-dependent change in the measured response is visible at higher drive levels. Since compression was also present in the measurement chain, this measurement should not be interpreted as a determination of the DUT $P_{1\text{dB}}$.

4.5 Answers to the Research Questions

Table 4.3 summarizes the result-level answer to each research question. Interpretations of the observed limitations and discrepancies are reserved for Chapter 5.

Table 4.3: Concise summary of the results corresponding to the research questions in Section 1.4.

RQ	Result
RQ1	The complete 225 MHz to 520 MHz tuning range was demonstrated in simulation. The simulated fractional bandwidth was approximately 4.9 % to 5.3 %, with insertion loss of approximately 3.6 dB to 5.5 dB. Full experimental validation across all switch states was not possible.
RQ2	The measured prototype reproduced the general resonant behavior of the corresponding modified simulation, but the measured resonances were shifted downward by approximately 10 %.
RQ3	The maximum continuous-wave and peak RF power handling of the DUT could not be determined with the available measurement setup.
RQ4	The measurements did not establish an intrinsic power limitation of the GaN switches; the final prototype measurements were affected by the surrounding implementation and the reworked hardware configuration.

5

Discussion and Conclusion

5.1 Main Findings

This thesis investigated the feasibility of using GaN RF switches in a tunable high-power band-pass filter covering approximately 225 MHz to 520 MHz. A second-order switched filter bank was designed, simulated, fabricated, and experimentally characterized. The work included ideal circuit synthesis, component-model-based simulation, EM simulation of critical PCB structures, evaluation-board measurements, prototype assembly, troubleshooting, and power testing.

The results indicate that GaN RF switches remain a promising alternative to PIN-diode switching networks for tunable RF filters. Measurements on the evaluation board were broadly consistent with the supplied engineering model, and the simulated complete filter bank reached the intended tuning range with approximately 5 % fractional bandwidth. However, the fabricated prototype could not validate the complete filter bank because several switches failed and the final measured board was partially reworked.

The most important outcome is therefore diagnostic rather than demonstrative. The final prototype showed resonant behavior similar to the simulation, but with an approximately 10 % downward frequency shift and degraded matching. Fault modeling showed that a shorted capacitor and additional parasitic capacitance could reproduce several measured features. Together with the grounding investigation and power tests, this indicates that the measured prototype was primarily limited by the passive network, RF grounding, layout parasitics, and rework damage before any intrinsic limitation of the GaN switches could be established.

5.2 Quantitative Comparison with Target Specifications

Table 5.1 summarizes the main quantitative performance targets and compares them with the simulated and measured results obtained in this work. The commercial reference values and initial project aims are included to clarify which requirements were met in simulation and which could be evaluated experimentally.

The comparison shows that the simulated design was reasonably close to the in-

Table 5.1: Quantitative comparison between commercial reference values, project targets, simulated performance, and measured prototype results.

Parameter	Commercial / reference value	Project target	Simulated design	Measured prototype	Comment
Frequency range	225 MHz to 520 MHz filter bank	225 MHz to 520 MHz	Approximately 225 MHz to 520 MHz	Not fully verified	Full tuning range could not be measured because only two switches remained operational in the final prototype.
System impedance	50 Ω	50 Ω	50 Ω ports used in simulation	50 Ω measurement environment	Evaluation board and VNA measurements used a 50 Ω reference system.
Fractional bandwidth	≥ 5 % for the 225 MHz to 520 MHz target case	5 %	Approximately 4.9 % to 5.3 %	Not fully characterized	Simulated bandwidth was close to target, but the final hardware state did not allow complete bandwidth characterization across all states.
Insertion loss	< 4 dB ideal 225 MHz to 520 MHz target / ≤ 6.3 dB commercial reference	< 4.1 dB optimization target	Approximately 3.6 dB to 5.5 dB	Not representative of full design	Simulation partly met the target, but several states exceeded 4.1 dB. Final measurements were affected by switch failures and rework.
Return loss / reflection	> 10 dB target	$S_{11} < -10$ dB	Designed for $S_{11} < -10$ dB	Worse than simulation, especially at lower frequency	Measurements showed poorer matching than simulation, particularly in the lower-frequency response.
Rejection	> 22 dB at ±12% for the 225 MHz to 520 MHz target case	Shape factor < 6 and rejection target from specification	Approximately 22 dB to 27 dB	Not fully characterized	Simulated high- and low-side rejection were broadly within the intended range.
Tuning step size	≥ 1180 kHz	Not fixed in final optimization	Multiple switch states simulated	Not verified	Full-state measurement was not possible due to switch failures.
RF power handling, in-band	Commercial reference: 1 W; project ambition: > 5 W, preferably 10 W	> 5 W	Not directly power-validated in simulation	Not determined	Voltage-stress analysis indicated a possible passive-component limitation
RF power handling, out-of-band	Commercial reference: 5 W; project ambition: > 5 W, preferably 10 W	> 5 W	Not directly power-validated	Not fully characterized	Out-of-band power handling could not be properly evaluated with the final damaged and reworked prototype.
$P_{1\mathrm{dB}}$	Commercial reference: 29 dBm	> 37 dBm, ideally 40 dBm	Not determined	Not determined	Compression testing was not completed in a controlled single-frequency setup.
Main limiting factor	PIN-diode/control-voltage limitations in commercial concept	GaN switch and passive-network power handling	Passive losses and parasitics	Capacitor voltage rating, grounding, switch failures, and rework parasitics	The final limitation was the implemented passive network rather than a demonstrated GaN switch limit.

tended small-signal RF targets, especially in terms of frequency coverage, fractional bandwidth, and rejection. However, the measured prototype could not be used to validate the complete tunable filter bank because several switches failed and the final measurements were performed on a partially functional, reworked board.

The implemented prototype could not be tested up to the intended 5 W power-handling target. The available measurement setup limited the test power to approximately 0.5 W. At this power level, the apparent input-referred compression point of the complete measurement chain decreased by approximately 0.5 dB to 1 dB. This change may indicate a power-dependent effect in the system, but it may also result from reflections or compression elsewhere in the measurement chain. Voltage stress across the filter capacitors at the high-impedance switch nodes was identified as another potential limitation at higher power. Consequently, the measurements do not establish the intrinsic power limit of the GaN switches.

5.3 Sources of Discrepancy Between Simulation and Measurement

The measured prototype response differed from the simulated response in both center frequency and matching. The most visible difference was an approximately 10 % downward frequency shift. Several mechanisms may have contributed to this discrepancy.

First, the switch-node and capacitor-bank layout introduced additional parasitic capacitance that was not fully represented in the first circuit-level simulations. Since the filter response is strongly dependent on small capacitance values, even sub-picofarad parasitic contributions can shift the resonant frequency noticeably.

Second, the RF grounding of the prototype was initially incomplete. This changed the return-current path and modified the effective inductance and capacitance of the resonant structure. After the grounding connection was repaired, the measured response became qualitatively closer to the simulated response.

Third, repeated switch failures and manual rework introduced additional uncertainty. Removed switches, replacement wires, damaged pads, and unintended solder bridges changed the electrical structure of the prototype. These effects were partially reproduced by fault modeling, where a shorted capacitor and added parasitic capacitances improved agreement between simulation and measurement.

The discrepancy should therefore not be interpreted as a failure of the GaN switch model alone. Instead, the results indicate that the complete physical implementation, especially grounding and parasitic capacitance in the switch-node region, dominated the measured behavior.

5.4 Conclusion

The work supports the feasibility of GaN-switched tunable RF filters at the concept level, but it does not constitute a full validation of a high-power 225 MHz to 520 MHz filter bank. The simulation results show that the chosen architecture can meet much of the small-signal RF target space. The prototype results show that the practical implementation was limited by grounding, parasitic capacitance, and assembly robustness before the GaN switches themselves could be fairly power-tested. Furthermore, capacitor voltage stress was identified as a potential limitation of a future high-power implementation; however, the limiting mechanism was not experimentally isolated in the present prototype.

A revised design using higher-voltage capacitors, lower switch-node impedance, improved RF grounding, and a simpler staged prototype would be required for a fair power-handling comparison against established PIN-diode-based implementations.

5.5 Future Work

Future work should begin with a simplified prototype containing only one GaN switch and one resonant section. This would make it possible to isolate switch behavior from filter-bank complexity and reduce the number of possible failure mechanisms.

A revised design should use capacitors with higher RF voltage ratings. The results of this thesis identify capacitor voltage stress as a potential limitation of the implemented design, although the ultimate power-limiting mechanism was not experimentally isolated. Components rated for at least 100 V should be considered for testing above 5 W.

The switch-node impedance should also be reduced. The implemented structure produced an impedance of approximately 200 Ω, which increased the voltage stress on the capacitors and switches. A topology with lower impedance or fewer switched capacitive branches could improve power handling.

The PCB design should include more robust RF grounding and clearer design-rule checks for all manually implemented ground connections. Ground continuity should be verified before soldering active components.

Finally, power testing should be performed using single-frequency excitation at the passband center rather than only swept VNA measurements. This would allow more controlled thermal and nonlinear characterization of the filter under realistic operating conditions.

Bibliography

[1] D. M. Pozar, *Microwave and RF Design of Wireless Systems.* New York: Wiley, 2001, ISBN: 978-0471322821.

[2] G. L. Matthaei, L. Young, and E. M. T. Jones, *Microwave Filters, Impedance-Matching Networks, and Coupling Structures.* New York: McGraw-Hill, 1964.

[3] J.-S. Hong and M. J. Lancaster, *Microstrip Filters for RF/Microwave Applications.* New York: Wiley, 2001, ISBN: 978-0471388773.

[4] J. Uher and W. J. R. Hoefer, "Tunable microwave and millimeter-wave band-pass filters," *IEEE Transactions on Microwave Theory and Techniques*, vol. 39, no. 4, pp. 643–653, Apr. 1991. DOI: 10.1109/22.76427

[5] P. W. Wong and I. C. Hunter, "Electronically tunable filters," *IEEE Microwave Magazine*, vol. 10, no. 6, pp. 46–54, Oct. 2009. DOI: 10.1109/MMM.2009.933593

[6] J.-S. Hong, "Reconfigurable planar filters," *IEEE Microwave Magazine*, vol. 10, no. 6, pp. 73–83, Oct. 2009. DOI: 10.1109/MMM.2009.933590

[7] X. Wu, J. Wang, J. Ye, J. Sun, and G. Hua, "Switched integrated band-pass filter bank utilizing 0.25-μm pHEMT GaAs process for S-, C-, and X-band applications," *IEICE Electronics Express*, vol. 21, no. 5, p. 20 230 624, 2024. DOI: 10.1587/elex.21.20230624

[8] D. Lu, J. Liu, and M. Yu, "Highly-selective bandpass switch block with applications of MMIC SPDT switch and switched filter bank," *IEEE Solid-State Circuits Letters*, vol. 5, pp. 190–193, 2022. DOI: 10.1109/LSSC.2022.3194410

[9] J. Yang and Z. Gao, "A tunable 0.2–1.2-GHz N-path bandpass filter with improved harmonic and out-of-band rejection," *IEEE Transactions on Microwave Theory and Techniques*, vol. 73, no. 9, pp. 6363–6371, 2025. DOI: 10.1109/TMTT.2025.3558245

[10] N. Desta and E. Cohen, "A bootstrapped 250-nm GaN MMIC N-path filter with a 31 dbm in-band P1dB," *IEEE Solid-State Circuits Letters*, vol. 7, pp. 66–69, 2024. DOI: 10.1109/LSSC.2024.3358083

[11] T. S. Alvi et al., "A high-performance, low-cost, and integrated hairpin topology RF switched filter bank for radar applications," *Sensors*, vol. 24, no. 2, p. 434, 2024. DOI: 10.3390/s24020434

[12] X. Wei, Y. Miao, X. Jin, T. H. Loh, and G. Liu, "Design of a novel SiP integrated RF front-end module based on SOI switch and SAW filter," *Sensors*, vol. 24, no. 21, p. 6994, 2024. DOI: 10.3390/s24216994

[13] R. H. Caverly and G. Hiller, "Establishing the minimum reverse bias for a p-i-n diode in a high-power switch," *IEEE Transactions on Microwave Theory and Techniques*, vol. 38, no. 12, pp. 1938–1943, Dec. 1990. DOI: 10.1109/22.64577

[14] MACOM Technology Solutions, "Establishing the minimum reverse bias for a pin diode in a high-power switch," MACOM Technology Solutions, Application Note AN3022, Revision V2. [Online]. Available: https://cdn.macom.com/applicationnotes/AN3022.pdf

[15] Netcom, Inc., *Model 5588 – tunable filter 30–520 mhz*, https://netcominc.com/products/5588-3/, Revision 0622018, 2018.

[16] Netcom, Inc., *Model 5590: 30–520 mhz digitally tunable filter*, Product specification, revision 06222018, Netcom, Inc., 2018. [Online]. Available: https://netcominc.com/products/5590-3/

[17] A. Ø. Olsen, *Personal communication*, Conversation with RF engineer, Personal communication, Feb. 2026.

[18] C. F. Campbell and D. C. Dumka, "Wideband high power gan on sic spdt switch mmics," in *2010 IEEE MTT-S International Microwave Symposium*, 2010, pp. 145–148. DOI: 10.1109/MWSYM.2010.5517940

[19] I. Lahbib, F. Drillet, J. Loraine, H. Saleh, O. Sow, and G. D. U'Ren, "Low insertion loss sub-6 GHz heterogeneous GaN/RF-SOI SPDT switch for high power applications," in *2023 IEEE/MTT-S International Microwave Symposium – IMS 2023*, 2023, pp. 343–346. DOI: 10.1109/IMS37964.2023.10188193

[20] P. Cardinael et al., "Contribution of substrate harmonic distortion to GaN-on-Si RF switches linearity," *IEEE Microwave and Wireless Technology Letters*, vol. 34, no. 3, pp. 298–301, 2024. DOI: 10.1109/LMWT.2024.3355148

[21] D. Frey, D. Matlock, E. Gebara, and N. C. Miller, "A temperature-dependent linear RF switch model for common-gate high-frequency GaN HEMT transistors," *International Journal of Numerical Modelling: Electronic Networks, Devices and Fields*, vol. 38, no. 4, e70084, 2025. DOI: 10.1002/jnm.70084

[22] J.-H. Lee, J.-W. Choi, X.-G. Wang, and S.-W. Yun, "Design of tunable bandpass filter using pin diode with constant absolute bandwidth," in *2013 Asia-Pacific Microwave Conference Proceedings (APMC)*, 2013, pp. 191–193. DOI: 10.1109/APMC.2013.6695090

[23] TagoreTech Inc., *TS63430D 50 W 4-Throw Tuning RF Switch (30 MHz to 1000 MHz): Product Brief*, Revision 0.35, Electrical specifications include typical $R_{\mathrm{on}} = 0.50\,\Omega$ and $C_{\mathrm{off}} = 500\,\mathrm{fF}$, 2026. Accessed: Aug. 23, 2026. [Online]. Available: https://tagoretech.com/Product_Doc/TS63430D.pdf

A

Supplementary Reproducibility Notes

This appendix records practical details that are useful when repeating or extending the prototype work. It does not introduce new measurements beyond those discussed in the main text.

Prototype status during final measurements

The final measured prototype was not the original full filter-bank implementation. Several GaN switches had failed during assembly and troubleshooting, and the final comparison was made on a partially reworked board with only the C8 switching path remaining partially operational. Consequently, the final measurements should be interpreted as diagnostic measurements of resonant behaviour, parasitic effects, and power-related changes, not as a complete validation of all switching states.

Recommended bring-up checklist

For a repeated design iteration, the following checks should be completed before RF power testing:

1. Verify DC current consumption for each switch state before connecting RF power.
2. Check RF ground continuity from the SMA connector grounds to the resonator and switch-node ground pads.
3. Measure the unpowered small-signal response of passive test structures before mounting active switches where possible.
4. Start with a single-switch or single-resonator test coupon before assembling a complete filter bank.
5. Record the exact attenuation and amplifier chain used during power testing so that card input power can be reconstructed unambiguously.

Design checks for future iterations

Future layouts should include an explicit RF-voltage-stress calculation for each switched capacitor state. The high-impedance switch node in this prototype increased capacitor voltage for a given input power, so capacitor voltage rating should be treated as a primary design constraint rather than a late-stage component-selection detail.

DEPARTMENT OF MICROTECHNOLOGY AND NANOSCIENCE
CHALMERS UNIVERSITY OF TECHNOLOGY
Gothenburg, Sweden
www.chalmers.se

CHALMERS
UNIVERSITY OF TECHNOLOGY